NOMAD spectrometer on the ExoMars trace gas orbiter mission:

part 1—design, manufacturing and testing of the infrared channels

Eddy Neefs [1](*), Ann Carine Vandaele [1], Rachel Drummond [1], Ian Thomas [1], Sophie Berkenbosch [1], Roland Clairquin [1], Sofie Delanoye [1], Bojan Ristic [1], Jeroen Maes [1], Sabrina Bonnewijn [1], Gerry Pieck [1], Eddy Equeter [1], Cédric Depiesse [1], Frank Daerden [1]; Emiel Van Ransbeeck [2]; Dennis Nevejans [3]; Julio Rodriguez [4], J.-J. Lopez-Moreno [4], Rosario Sanz [4], Rafael Morales [4], Gian Paolo Candini [4], Carmen Pastor [4], Beatriz Aparicio del Moral [4], José-Maria Jeronimo [4], Juanma Gomez [4]; Isabel Perez [5], Fermin Navarro [5], Javier Cubas [5], Gustavo Alonso [5], Alejandro Gomez [5]; Tanguy Thibert [6]; Manish Patel [7]; Giancarlo Belucci [8]; Lieve De Vos [9], Stefan Lesschaeve [9], Nico Van Vooren [9], Wouter Moelans [9], Ludovic Aballea [9], Stijn Glorieux [9], Ann Baeke [9], Dave Kendall [9], Jurgen De Neef [9], Alexander Soenen [9], Pierre-Yves Puech [9]; Jon Ward [10]; Jean-François Jamoye [11]; David Diez[12], Anna Vicario [12]; Michel Jankowski [13]

Affiliations

[1] Belgian Institute for Space Aeronomy, BIRA-IASB, Ringlaan 3, 1180 Brussels, Belgium
[2] VREC, Dries 15, 1745 Mazenzele, Belgium
[3] CONSERD, Krekelstraat 27, 9052 Gent, Belgium
[4] Instituto de Astrofisica de Andalucia, IAA-CSIC, Glorieta de la Astronomia, 18008 Granada, Spain
[5] Instituto Universitario Ignacio Da Riva c/o ETSI Aeronauticos, IDR-UPM, 28040 Madrid, Spain
[6] Centre Spatial de Liège, CSL, Liège Science Park, avenue du Pré-Aily, 4031 Angleur, Belgium
[7] Open University, PSSRI-OU, Walton Hal, Milton-Keynes, MK76AA, United Kingdom
[8] Istituto di Fisica dello Spazio Interplanetario, IFSI, Via del Fosso del Cavaliere 100, 00133 Rome, Italy
[9] OIP, Westerring 21, 9700 Oudenaarde, Belgium
[10] Gooch and Housego, Dowlish Ford, Ilminster, TA19 0PF, United Kingdom
[11] AMOS, rue des Chasseurs Ardennais 2, 4031 Angleur, Belgium
[12] ERZIA, Castelar 3, 39004 Santander, Spain
[13] Thales Alenia Space, ETCA, rue Chapelle Beaussart 101, 6032 Mont-sur-Marchienne, Belgium
[*] Correspondence to eddy.neefs@aeronomie.be

Key Words

ExoMars, Trace Gas Orbiter, spectrometer, solar occultation, nadir, echelle grating, acousto-optical tunable filter

Abstract

NOMAD is a spectrometer suite on board ESA's ExoMars Trace Gas Orbiter (TGO) due for launch in January 2016. NOMAD consists of two infrared channels and one ultraviolet and visible channel allowing the instrument to perform observations quasi constantly, by taking nadir measurements at day- and nightside, and during solar occultations. In this paper the pre-launch activities (design, manufacturing and testing) of the infrared channels are described. Focus is put on the optical working principle in these channels, where an echelle grating, used as diffractive element, is combined with an acousto-optical tunable filter (AOTF), used as diffraction order sorter.

Introduction

On November 9th 2005 Venus Express was launched, an ESA mission aiming for a broad scientific analysis of Venus, one of Earth's sister planets. On board the Venus Express spacecraft was the SPICAV instrument (Spectroscopy for the Investigation of the Atmosphere of Venus) that was built in close collaboration between the Belgian Institute for Space Aeronomy (BIRA-IASB), Belgium, the Service d'Aéronomie of the CNRS, France and the Institute for Space Research, Russia. SPICAV contained three optical spectrometers one of which was the Belgian SOIR-channel (Solar Occultations in the Infrared), a compact high-resolution echelle grating spectrometer with acousto-optical tunable filter for the infrared domain between 2.3 and 4.3 µm [1].

At the time of the redaction of this article (end 2014) Venus Express is still active. SOIR, that produced a first absorption spectrum in May 2006, has since then delivered a wealth of data on the chemical composition of the Venus atmosphere [2,3,4]. Over a period of nearly ten years of intensive operation in space, SOIR has shown no sign of degradation and will most probably continue operations until an end is set by ESA to this highly successful mission or the spacecraft runs out of fuel.

With SOIR an unprecedented spectral resolution was obtained for an infrared optical spectrometer measuring infrared absorption spectra in a planetary atmosphere other than the Earth [5,6,7]. It has an instrument line profile (ILP) of 0.22 cm^{-1} FWHM or better over its complete wavelength range (sampled by 2 pixels). This is an order of magnitude higher than any other existing comparable instrument. While SOIR offers an interesting spectral resolution, it has the additional advantage of not being a very bulky instrument (less than 7 kg). SOIR's low weight was achieved by utilizing a coarse spaced echelle grating, a highly dispersive element operated at high diffraction orders , in combination with an acousto-optical tunable filter (AOTF), used as an order sorting device in front of the diffraction section. Its reduced weight and the fact that no moving parts are needed to scan through the targeted wavelength domain, makes SOIR-like instruments very appropriate for interplanetary missions, that in general have limited resources [8,9,10].

Although echelle-AOTF combinations were flown in space for the ultraviolet-visible (200 to 425 nm) [11,12,13] and the near infrared domain (1 to 1.65 µm) [14,15], SOIR was the first instrument to successfully use the technique in the wider infrared range between 2.2 and 4.3 µm.

The concept of the SOIR instrument was initially designed for observations of planet Mars, but due to budgetary reasons it could not be withheld for the Mars-Express payload [16]. It first flew to Venus [17], proving there its usefulness and versatility. Nevertheless, SOIR's spectral range remains extremely well suited for atmospheric studies in the Mars atmosphere, since it encompasses amongst others the main absorption line of methane (3.3 µm – 3000 cm^{-1}), the detection and localization of which is one of the most important goals in Martian science today.

BIRA-IASB was supported strongly by Belgian Science Policy (BELSPO) to propose SOIR when in 2010 ESA and NASA jointly called for ideas for their double ExoMars mission with launches in 2016 (orbiter plus entry, descent and landing demonstrator module) and 2018 (lander with rover), hoping to catch up the missed opportunity of flying SOIR on Mars-Express.

NOMAD (Nadir and Occultation for Mars Discovery), the instrument that was proposed for ExoMars, is an integrated suite of three spectrometers. The first is called SO (Solar Occultations) and has

exactly the same optical design as SOIR, an infrared echelle-AOTF spectrometer in the 2.3 to 4.3 µm range with a resolving power at mid-range of approximately $\lambda/\Delta\lambda$=20,000, using uniquely the solar occultation technique. It was proven during the Venus-Express mission that, although SOIR does a great job as solar occultation instrument, its signal-to-noise ratio is too low when observing at limb or nadir. The contribution of thermal background in SOIR's wavelength domain drowns the weaker signal.

Therefore a second channel was added to the NOMAD suite, called LNO (Limb, Nadir and Occultations). Conceptually it is identical to SOIR (and NOMAD's SO-channel) but it has been optimized for observing weak light sources. Compared to SO, LNO has a slightly reduced wavelength domain (between 2.3 and 3.8 µm) and a resolving power at mid-range of approximately $\lambda/\Delta\lambda$=10,000.

As a complement to the more bulky infrared SO and LNO-channels, a third spectrometer, called UVIS, has been integrated in the NOMAD instrument. UVIS is also based on heritage. It builds on a UK contribution to the Humboldt payload on the original ExoMars lander [18], a program that was stopped in 2009. BIRA-IASB has teamed up with the Open University (OU), UK, to adapt the concept for an orbiter mission, and making it capable of measuring in nadir, limb and solar occultation mode. It ranges from 200 nm in the ultraviolet up to 650 nm in the visible, and offers a spectral resolution better than 2 nm. The UVIS-channel is based on a Czerny-Turner layout, a totally different spectrometer concept than the infrared channels. The addition of dual front-end telescopic viewing optics transforms UVIS from a surface instrument to an orbital instrument with minimal modifications. Only an overview of the characteristics of the UVIS-channel will be discussed here. Further technical details on the implementation are described in a separate paper [19].

When NASA abandoned the ExoMars program in 2012, ESA partnered up with the Russian space agency ROSCOSMOS rescuing this challenging mission. While, as a consequence of this new partnership, Russian instruments came to replace earlier US contributions, NOMAD stayed on board as the only fully European payload. The launch of the Trace Gas Orbiter (TGO), the first segment of ExoMars, has been maintained and is scheduled for January 2016.

ExoMars Mission and NOMAD Scientific Goals

The Joint Instrument Defintion Team of ESA and NASA for the 2016 ExoMars TGO mission [20] earmarked in its example payload a solar-nadir-limb infrared mapper with highest priority. NOMAD corresponds to the description of this instrument and addresses three of the four TGO mission science goals.

NOMAD will look for atmospheric markers of life in the Martian atmosphere, identify potential source regions and provide information on the nature of the processes involved. NOMAD will study the major climatological cycles such as water, ozone and carbon cycles, the components and isotopes involved, and their escape from the atmosphere. NOMAD will also look for traces of active geology and volcanism on Mars. Consequently the three key science objectives for NOMAD have been defined as follows.

(1) Play an important role in the analysis of the chemical composition of the Martian atmosphere by detecting trace gases, such as CO_2, CO, H_2O, HO_2, NO_2, N_2O, CH_4, C_2H_2, C_2H_4, C_2H_6, H_2CO, HCN, H_2S, OCS, HCl (SO and LNO-channels) and SO_2, O_3 (UVIS-channel), and

isotopes, such as $^{13}CO_2$, ^{17}OCO, ^{18}OCO, $C^{18}O_2$, ^{13}CO,$C^{18}O$, HDO, $^{13}CH_4$, CH_4D, not only in the lower and middle atmosphere, but also in the upper atmosphere. Contribute to the comprehension of the past and future evolution of the atmosphere by studying the escape processes at the edge between atmosphere and space. Constrain especially the origin of methane and its destruction. Study gases that relate to ongoing geophysical and volcanic activity.

(2) For the above mentioned trace gases, characterize their spatial and temporal variations. Refine the present knowledge of CO_2-, CO-, H_2O- and O_3-climatologies, and in general of atmospheric dynamics.

(3) For the above mentioned trace gases, characterize their production and loss mechanisms, and localize their sources. Refine the present knowledge of water, carbon, ozone and dust cycles, and their relation to surface mineralogy and polar ice formation.

The science objectives of NOMAD are described in a separate paper [21].

Spectrometer Design Objectives

The SO-channel

Since the SO-channel of NOMAD builds strongly on heritage of SOIR, its design objectives are kept unchanged. The spectral observation band has to cover the 2.3 to 4.3 µm range, the ILP goal is set to 0.22 cm^{-1} FWHM or better over the whole spectral range, to be sampled by at least 2 detector pixels. Given the importance of detecting methane (absorption line around 3000 cm^{-1}), the instrument has to be optimized close to that wavenumber, resulting in an ILP of 0.15 cm^{-1} FWHM @ 3.3 µm.

The field of view (FOV) of the SO-channel is fully defined by the fact that it has to observe solely during solar occultation. The SOIR FOV for the spatial dimension of 30 arcmin is maintained although the maximum apparent diameter of the Sun at Mars is considerably smaller (23 arcmin) compared to Venus (44 arcmin). It is required that all the detector lines illuminated by the solar disk can be downloaded to Earth. Perpendicular to the spatial direction a FOV of 2 arcmin is maintained resulting in sufficient height resolution while scanning through the Martian atmosphere (vertical sampling ≤ 1 km). From dimensional constraints it follows that the entrance aperture diameter of the SO-channel shall be at maximum 20 mm.

Table 1. Summary of SO-channel specifications.

Characteristic	Value or Range	Unit
Wavelength λ	2.3 – 4.3	µm
Wavenumber	4250 – 2320	cm^{-1}
Instrument Line Profile (ILP)	0.22	cm^{-1}
• ILP for CH_4	0.15	cm^{-1}
Pixel sampling (FWHM)	≥ 2	
Polarization	linear, parallel to slit	
Resolving power $\lambda/\Delta\lambda$	20000	
Slit width in object space	2	arcmin
Slit length in object space	30	arcmin x arcmin
Field of View	2 x 30	
Spatial sampling	1	arcmin
Vertical sampling	≤ 1	Km
SNR	≥ 900	
Mass (incl all NOMAD electronics)	13.5	Kg
Dimensions (without periscope)	490.5 x 353 x 208	mm^3

SO shall have a signal-to-noise ratio (SNR) ≥ 900 over the complete spectral range, measured over a zone of 200 detector columns centred on the column with the maximum signal, for a minimum solar signal (i.e. at maximum Mars-Sun distance) and including all instrument sources of noise. Table 1 gives an overview of the characteristics of the SO-channel.

The LNO-channel

The SO-channel is not sensitive enough to observe the atmosphere using faint light sources (Martian disk and limb). Taking into account the fact that an instrument with an overall mass around 28 kg was allowed, it was decided, rather than to modify the SO-channel drastically and, hence, losing the heritage from SOIR in that channel, to add a second channel, on top of the first, that can observe with all light sources (Limb, Nadir and Occultation). This LNO-channel has the additional advantage that it can serve as backup in case the SO-channel would fail.

For LNO, operating in solar occultation mode, the same design objectives are valid as for the SO-channel. It is clear that the most challenging design objectives are situated in the nadir and limb mode of this channel. More than the spectral characteristics, the SNR is set out here to be the main design driver. An SNR of ≥ 400 is required over the complete spectral domain, after binning of all detector rows by column, measured over a zone of 200 columns centred on the column with the maximum signal, for a minimum solar signal (i.e. at maximum Mars-Sun distance), and including all instrument sources of noise. In the region that contains the methane absorption line, an SNR of ≥ 1000 is specified.

As a price to pay for the challenging SNR specification, design objectives on wavelength domain (between 2.3 and 3.8 μm) and ILP (0.5 cm^{-1}, sampled by at least 2 pixels) are relaxed, but are still in line with the scientific goals of the instrument.

Table 2. Summary of LNO-channel specifications.

Characteristic	Value or Range	Unit
General		
Wavelength λ	2.3 – 3.8	μm
Wavenumber	4250 – 2630	cm^{-1}
Instrument Line Profile (ILP)	0.5	cm^{-1}
Pixel sampling (FWHM)	≥ 2	
Polarization	linear, parallel to slit	
Resolving power $\lambda/\Delta\lambda$	10000	
Slit width in object space	4	arcmin
Slit length in object space	150	arcmin
Field of View	4 x 150	arcmin x arcmin
Spatial sampling	1	arcmin
Entrance aperture diameter	29.5 x 24	mm^2
Mass	9.4	kg
Dimensions (without periscope)	445 x 327 x 182	mm^3
Solar occultations		
Vertical sampling	≤ 1	km
SNR	≥ 900	
Nadir		
Footprint (400 km orbit)	60 x 0.3	$arcmin^2$
	60 x 17.5	km^2
SNR	≥ 400	
• SNR for CH_4	≥ 1000	

While defining an appropriate instantaneous FOV for the LNO-channel, a compromise had to be found between the channel performance in solar occultation (vertical sampling) and in nadir mode (SNR, footprint). In the assumption that the spacecraft is at 400 km above the surface, that the line of sight (LOS) moves along track with a velocity of approximately 3 km/s, that the orientation of the instantaneous FOV is variable, and that the maximum measurement time is 15 s, the footprint of the LNO FOV on the surface shall not be larger than 1° by 0.3° or 51 km by 17.5 km. This requirement is met with a FOV of the LNO-channel of 150 arcmin by 4 arcmin. Since LNO uses this FOV also for solar occultations, the vertical sampling capacity of LNO will be reduced by a factor of 2 compared to the SO-channel. The entrance aperture diameter of the LNO-channel shall be maximum 30 mm, which is higher than for the SO-channel, to allow for higher signal input. Table 2 gives an overview of the characteristics of the LNO-channel.

Both in the SO- and the LNO-channel the presence of ghost peaks and straylight, as well as optical aberrations such as tilt, smile and frown, shall be minimized as much as possible.

The UVIS-channel

The spectral range that was set forward for UVIS's predecessor on Humboldt (ExoMars lander) is maintained (200 to 650 nm). For the ExoMars orbiter mission a spectral resolution ≤ 10 nm is acceptable. It has been proven however from heritage that UVIS can have a spectral resolution better than 2 nm over its complete range. This latter value has been used as design objective.

When UVIS is measuring in solar occultation mode, its SNR requirement are set to ≥ 1000 (230 to 450 nm) and ≥ 500 (450 to 650 nm). In nadir mode the SNR requirement are set to ≥ 500 (230 to 450 nm) and ≥ 250 (450 to 650 nm), always taking into account all internal noise sources and for a minimum solar signal.

Table 3. Summary of UVIS-channel specifications.

Characteristic	Value or Range	Unit
General		
Wavelength λ	200 - 650	nm
Wavenumber	50000 - 15400	cm^{-1}
Spectral resolution	≤ 2	nm
SNR	≥ 900	
Mass	0.95	kg
Dimensions (without periscope)	143 x 170 x 118	mm^3
Solar occultation		
Circular FOV	2	arcmin
Vertical sampling	≤ 1	km
Entrance aperture diameter	20.5	mm
SNR (230 - 450 nm)	≥ 1000	
SNR (450 - 650 nm)	≥ 500	
Nadir		
Circular FOV	43	arcmin
Entrance aperture diameter	26	mm
Footprint (400 km orbit)	60 x 5	$arcmin^2$
	60 x 5	km^2
SNR (230 - 450 nm)	≥ 500	
SNR (450 - 650 nm)	≥ 250	

The solar FOV of UVIS has to be compliant with the general solar occultation objective of attaining a vertical sampling of the atmosphere of at least 1 km. Therefore a circular FOV of 2 arcmin is proposed, which is in line with the FOV of the SO-channel. Under the same assumptions as for the LNO-channel in nadir mode (400 km above surface, spacecraft speed of 3 km/s, maximum

measurement time of 15 s) the footprint of UVIS FOV on the surface of Mars shall not be larger than 60 arcmin by 5 arcmin or 80 km by 5 km). This requirement is met for a circular FOV of the UVIS-channel of 43 arcmin. The entrance aperture diameter of UVIS is 20.5 mm for the solar viewport and 26 mm for the nadir viewport. Table 3 gives an overview of the characteristics of the UVIS-channel.

General Design Rules

ExoMars TGO is a nadir tracking spacecraft, meaning that its –Y-axis is always pointing towards and perpendicular to the surface of Mars. NOMAD has two nadir lines of sight (one in the LNO- and one in the UVIS-channel) that are parallel to this axis. Therefore NOMAD's nadir viewports are always directed to Mars. The orbital configuration of ExoMars fixes the angle between its -Y-axis and the direction of the Martian limb to 67.07° away from the –Y-axis in the –Y/–X-plane. NOMAD's three solar lines of sight (one in each of the channels) will be parallel to this limb direction, and hence form an angle of 67.07° with the nadir lines of sight. To perform solar occultation measurements, the S/C will need to yaw rotate around its Y-axis twice per orbit, once during the day, once during the night, so that, well before sunrise or sunset, the solar lines of sight point to the limb. During solar occultations the spacecraft will adopt an inertial pointing mode, fixed on the center of the Sun, resulting in an apparent ingress into or egress from the Martian disk. The morphology of ExoMars TGO is therefore naturally suited to perform nadir and limb observations, and additionally offers the possibility to measure during solar occultations, when NOMAD's solar lines of sight pass through the atmosphere just before sunset or just after sunrise (Figure 1).

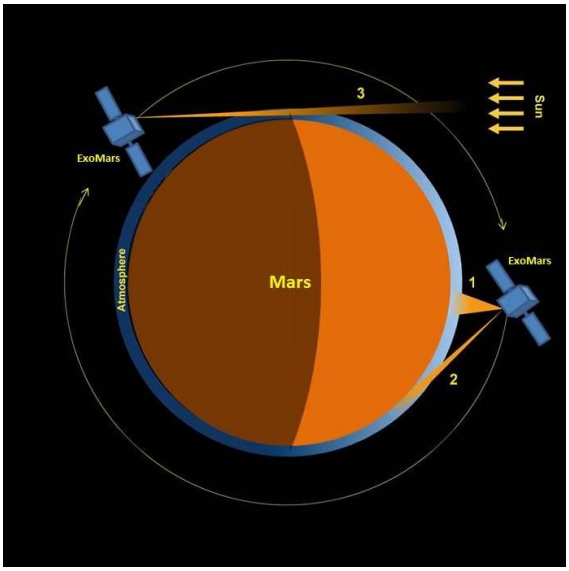

Figure 1. Different observation modes with NOMAD in orbit around Mars (1 = nadir, 2 = limb, 3 = solar occultation).

To fulfil NOMAD's science goals during solar occultations, the SO-, LNO- and UVIS-channels must observe as similar a slice of the atmosphere as possible. To maximize the signal, the SO- and LNO-channel fields of view must comprise the entire solar disc and the UVIS-channel FOV must be as central as possible on the Sun. Therefore a good co-alignment between the 3 channels shall be assured throughout the lifetime of the instrument (Figure 2). It is required that each of the solar lines of sight is aligned to the instrument's mechanical axis with an accuracy of ≤ ±0.15 mrad. During nadir observations the footprints of the LNO and UVIS FOV shall overlap entirely, requiring an alignment accuracy with the mechanical axis of ≤ ±10 mrad.

Together with the NOMAD-to-spacecraft co-alignment accuracy (≤ ±0.2 mrad), the above mentioned internal co-alignment accuracies contribute to the overall pointing budget for NOMAD. Table 4 gives an overview of the requirements for the most important co-alignment contributions, while Table 5 gives an overview of the requirements for the absolute and relative pointing errors.

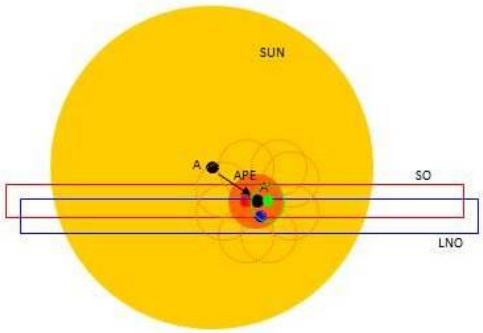

Figure 2. NOMAD channel co-alignment (A is center of the Sun; A' is pointing axis of spacecraft; APE is absolute pointing error; red rectangle is SO FOV; red bullet is SO LOS; blue rectangle is LNO FOV; blue bullet is LNO LOS; green circle is UVIS FOV; green bullet is UVIS LOS; orange target is maximum allowed misalignment between all LOS (including ACS); dotted orange targets are maximum allowed spacecraft RPE).

Table 4. Co-alignment contributors.

Co-alignment contributors	Accuracy limit	Knowledge accuracy
Solar LOS to NOMAD mechanical axis	± 0.15 mrad	
Nadir LOS to NOMAD mechanical axis	± 10.0 mrad	
NOMAD mechanical axis to spacecraft axis	± 0.20 mrad	0.05 mrad
Any NOMAD solar LOS to spacecraft axis (1)	± 0.30 mrad	

(1) *it is assumed that the ACS-instrument, that performs solar occultation measurements at the same time as NOMAD, has a similar co-alignment budget of ±0.30 mrad, leading to a maximum misalignment between the NOMAD and ACS solar lines of sight of 0.60 mrad.*

Table 5. Pointing budget.

Pointing	Error limit	Knowledge accuracy
Absolute Pointing Error (APE) solar	≤ 1.23 mrad	
Relative Pointing Error (RPE) solar (short + long term) (2)	≤ 1.23 mrad	
Absolute Pointing Error (APE) nadir	≤ 3.50 mrad	
Relative Pointing Error (RPE) nadir (long term) (2)	≤ 3.00 mrad	
Relative Pointing Error (RPE) nadir (short term) (2)	≤ 0.54 mrad	
Overall pointing knowledge solar		≤ 0.45 mrad
Overall pointing knowledge nadir		≤ 0.54 mrad

(2) *short term is 1 s, long term is 60 s*

It is important to notice that the rectangular FOV of the SO- and the LNO-channel shall be aligned by the spacecraft perpendicular to the limb at a chosen altitude above the surface (Figure 3).

The length and width of the SOIR-channel on Venus-Express were imposed by the dimensions of the existing SPICAM-Light channel on top of which SOIR was built. As a consequence, the optical path of SOIR had to be compacted by adding a 90°-turn towards a detector assembly that was placed perpendicular to the base plate on a complicated mechanical mount. In the SO-channel of NOMAD this extra complication was avoided. The baseplate of the SO-channel is somewhat longer and wider than for SOIR, allowing to mount the detector assembly immediately to the base plate, with its optical axis in line with the optical axis of the spectrometer (footprint on spacecraft 490.5 x 353 mm^2).

As LNO is mounted on top of SO it was requested to have more or less the same length and width (footprint 445 x 327 mm^2). Since LNO's entrance aperture diameter is bigger, all its optical elements are larger, but still had to fit within the available area. The height above the optical bench of the SO- and LNO-channels is 118 mm and 136 mm respectively. The UVIS-channel had to be installed in a free area on the SO-base plate. This constrained its maximum dimensions to 143 x 170 x 118 mm^3. The abovementioned volumes are without the additional external primary mirrors (periscopes) needed to fold the solar lines of sight of SO, LNO and UVIS into the direction of the Sun (67.07°).

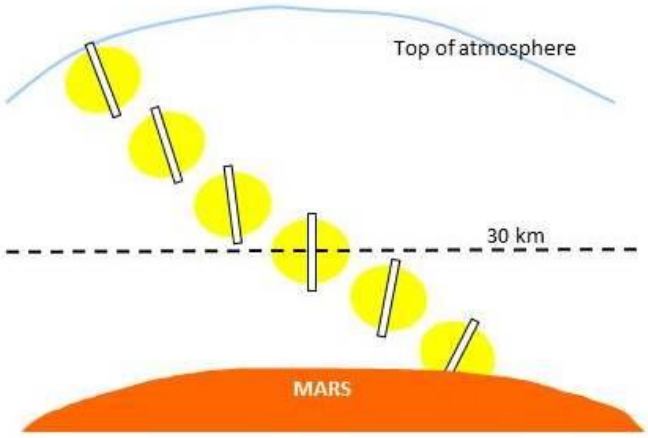

Figure 3. Example of slit orientation in Mars atmosphere (slit perpendicular to limb at 100 km altitude).

The maximum allowed weight for NOMAD, imposed by the spacecraft, is 28.86 kg including margins. From this, weight limits for the SO, LNO and UVIS optical benches were imposed of 13.35 kg (including all NOMAD electronics), 9.4 kg resp. 0.95 kg. The remaining mass (3.7 kg) was attributed to harnessing, MLI and instrument-to-spacecraft mounting hardware.

NOMAD has to survive in the environmental conditions imposed by the spacecraft. The most severe constraints are the operational (-30 to +50 °C) and non-operational (-40 to +60 °C) thermal limits.

Spectrometer Design

SO- and LNO-channels

With the above mentioned design objectives and maximum maintenance of SOIR heritage as drivers, it was decided to build both infrared channels around a high-dispersion echelle grating. To avoid overlap of orders at the output of the grating, acousto-optical tunable filters (AOTF, manufactured by Gooch&Housego, UK) are placed as order sorting devices in front of the spectrometer sections. We remind that the use of echelle gratings has the distinct advantage over other types of spectrometers (based e.g. on cross-orthogonal dispersion) that the full height of the detector can be used to register spectral lines, allowing to improve the SNR by column binning. AOTFs on the other hand offer a quick electronic driven random access to the spectral orders, with no need for moving mechanical parts, and with the possibility to use them as optical shutter, blocking incident light so that background measurements can be performed.

The optical principle, which is valid for the two channels, is given in Figure 4. The real optical layout of SO and LNO is shown in Figure 5 and Figure 6 respectively. The front end optics of the channels consists of the AOTF entrance optics (nr.3) that is a telescope matching the incoming light beam to

the acceptance angle of the AOTF. In the intermediate image plane of the entrance optics a diaphragm (nr.4) is placed that limits the FOV of the system in order to reduce scattering and ghost images, and to prevent overlap between order 1 and order 0 of the AOTF. In the LNO-channel an additional folding mirror (nr.5) had to be inserted between AOTF entrance optics and AOTF. An AOTF (nr.6) selects the order from the incoming light beam that corresponds to an RF-signal applied to the crystal, and outputs this small fraction of the beam towards the AOTF exit optics (nr.7). All other orders are blocked. Via a small folding mirror (nr.8) the AOTF exit optics creates an image of the scene (Sun or surface of Mars) on the spectrometer entrance slit (nr.9). The slit defines the FOV of the spectrometer. An off-axis parabolic mirror (nr.10) serves as collimating lens in the spectrometer section and offers a parallel light beam to the echelle grating (nr.11). After dispersion of the light by the grating, the beam passes again by the parabolic mirror (nr.10), now serving, together with the detector optics (nr.13), as imaging lens. Via a folding mirror (nr.12) the beam is projected on the detector (nr.14) that has its optical axis parallel to the overall optical axis of the channel. The spectral properties of the channels (free spectral range, instrument line profile) are accomplished by the choice of the configuration and characteristics of echelle grating, parabolic mirror and detector optics. To obtain the required spectral sampling interval of the system, also the pixel size of the detector is of importance.

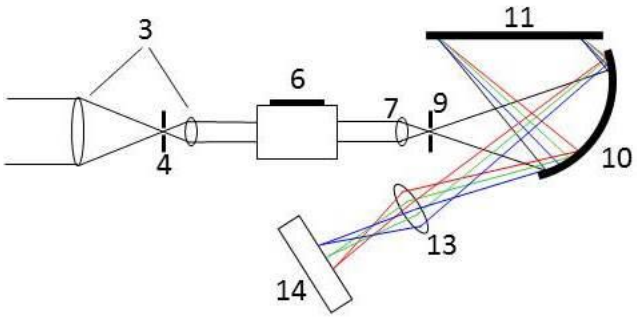

Figure 4. Optical principle of NOMAD's infrared channels channel.

The entrance of the SO-channel is a periscope consisting of three flat mirrors (nr.1 in Figure 5). The two mirrors inside the SO base plate are needed to shift the channel's aperture to a location where the incoming beam is not obstructed by other spacecraft elements. The third mirror is protruding outside the base plate and tilts the optical axis by 67.07° in the direction of the Martian limb.

The LNO-channel has two entrance apertures. The solar entrance is a periscope with two flat mirrors (nr.1 in Figure 6), one inside the base plate, one protruding and tilting the beam by 67.07°. The nadir entrance consists of one single flat flip mirror (nr.2). This mirror is driven by a motor and can be placed either inside the beam (nominal position, the LNO-channel looks at nadir) or outside the beam (the LNO-channel looks at the Sun).

Although the conceptual design of the SO- and LNO-channels is concurrent, some differences can be noticed. In the SO-channel, from heritage, the F-numbers of the optics (f/5.16) and the detector (f/3.936) are not matched, in LNO they are f/3.936 everywhere. While the focal length (103 mm) remains the same in the two channels, this means that the optical elements in LNO scale up in size by approximately 30%, and a higher spectrometer slit can be used, contributing positively to the SNR (see below).

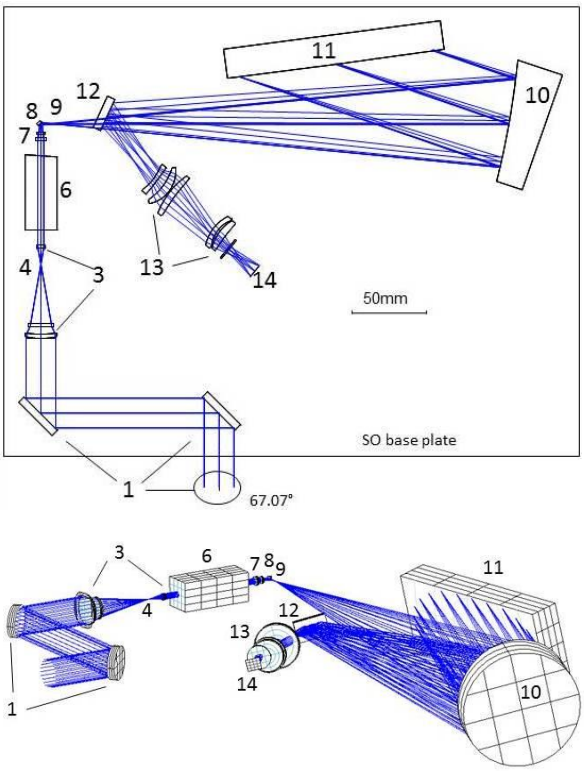

Figure 5. Optical design of the SO-channel (2D top; 3D bottom).

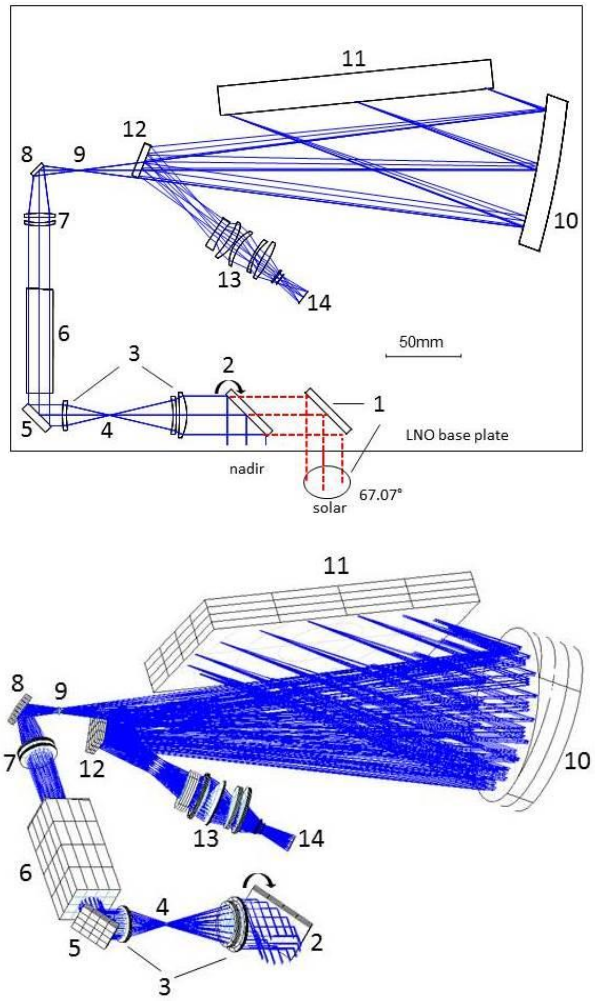

Figure 6. Optical design of the LNO-channel (2D top; 3D bottom).

In the SO-channel the limiting aperture of the system is the diaphragm in the AOTF entrance optics (f/# = f/5.16), while in the LNO-channel it is the cold shield of the detector (f/# = f/3.936). This means that in SO it is the entrance pupil (coincident with the first lens of the instrument) that is imaged along the optical path, and in LNO it is the exit pupil (coincident with the cold shield). Images of the respective pupils are formed at the first lens and the cold shield, but also at two other positions in the instrument: (1) in the middle of the AOTF to avoid vignetting of the spatial FOV at the entrance and exit of the crystal, and (2) on the grating, to keep its dimensions as small as possible. Table 6 gives an overview of the first order optical properties for the two channels.

Table 6. First order optical properties.

Parameter	SO	LNO	Unit
Entrance aperture	20 x 20 (circular)	29.5 x 24 (elliptical)	mm^2
Overall focal length	103		mm
Focal length optics in front of slit	103		mm
Magnification AOTF entrance optics	5X	1.85X	
Focal length AOTF entrance "objective"	58.4	57.0	mm
Focal length AOTF entrance "collimator"	11.6	30.7	mm
Focal length AOTF exit optics	20	55.8	mm
Magnification optics behind slit	1X		
Focal length collimating lens	300		mm
Focal length imaging lens	300		mm
Focal length parabolic mirror	300		mm
Magnification detector optics	1X		
Limiting F-number	f/5.12	f/3.936	

Grating and Imager Optical Properties

Free Spectral Range

For an echelle grating that is used in the Littrow configuration (incidence angle α and diffraction angle β are the same and equal to the blaze angle Θ_B) the grating equation is [22,23]:

$$m.\lambda_c = \frac{\sin\alpha + \sin\beta}{g} = \frac{2\cdot\sin\theta_B}{g} \quad \textit{(Equation 1),}$$

where g is the groove density (in lines/mm) of the grating, m the diffraction order and λ_c the central wavelength of order m.

The echelle gratings in the infrared channels of NOMAD are used in a “near” Littrow configuration. To separate the incident and diffracted beam, the gratings are slightly tilted such that both beams make a small angle γ with the plane that is perpendicular to the grating surface and the grooves. Besides that there is also a small deviation i of the angle of incidence from the blaze angle in the plane normal to grooves and surface. In these conditions the simplified grating Equation 1 has to be rewritten as:

$$m.\lambda_c = \frac{2\cdot\sin\theta_B\cdot\cos i\cdot\cos\gamma}{g} \quad \textit{(Equation 2).}$$

The spectrometer design and alignment of the NOMAD channels is such that the central wavelength λ_c of each order falls in the center of the detector.

The free spectral range *FSR*, the wavelength range in which there is no overlap by adjacent orders, is a constant for echelle gratings:

$$FSR = \frac{1}{\lambda_c . m} = \frac{g}{2 \cdot \sin\theta_B \cdot \cos i \cdot \cos\gamma} = Cte \quad \textit{(Equation 3).}$$

The wavelengths at the edges of the FSR can be derived from Equation 2 and Equation 3 as follows:

$$\lambda_0 = \lambda_c \pm \frac{FSR}{2} = \frac{2 \cdot \sin\theta_B \cdot \cos i \cdot \cos\gamma}{g \cdot \left(m \pm 1/2\right)} \quad \textit{(Equation 4).}$$

Table 7 gives an overview of the grating characteristics, Table 8 and Table 9 give for each channel the theoretical values of λ_c, λ_0^+ and λ_0^- for some orders.

Table 7. Grating characteristics.

Parameter	SO	LNO	Accuracy	Unit
Wavelength range	2.3 – 4.3	2.3 – 3.9		µm
Blaze angle Θ_B	63.43		±0.1	°
Groove density *g* (@ 24.5 °C)(1)	4.031283			lines/mm
Groove density *g* (@ 0 °C) (2)	4.033512			lines/mm
Number of lines N	≥593	≥765		
Groove spacing (@ 24.5 °C)(1)	248.06		±0.001	µm
Length of grooved area	N x 248.06		±0.1	µm
Off Littrow angle *γ*	2.6	2.75	±0.025	°
Off blaze angle *i*	-0.02	0	±0.016	°
Useful area	≥147.1 x 74.5	≥190 x (97.50-91.85) (3)		mm^2
Size (*L* x *W* x *T*)	148.1 x 96.84 x 25	191 x 123.5 x 40	±0.1	mm^3
Free spectral range *FSR*	22.56			cm^{-1}

(1) *manufacturing temperature;* (2) *goal operating temperature;* (3) *useful area is not fully rectangular*

Writing again the grating Equation 2 for the near-Littrow case of NOMAD, now for a diffracted beam at wavelength λ, making an angle φ with the diffracted ray at wavelength λ_c, the ray that defines the optical axis of the imager, we have:

$$m.\lambda = \frac{\left[\sin\left(\theta_B + i\right) + \sin\left(\theta_B - i - \varphi\right)\right].\cos\gamma}{g} \quad \textit{(Equation 5) .}$$

A special case of Equation 5 can be written for the rays at wavelengths λ_e^+ *and* λ_e^- that fall on the edges of the detector's sensitive area:

$$m.\lambda_e^+ = \frac{\left[\sin\left(\theta_B + i\right) + \sin\left(\theta_B - i + \Delta\varphi\right)\right].\cos\gamma}{g} \quad \textit{(Equation 6)}$$

and

$$m.\lambda_e^- = \frac{\left[\sin\left(\theta_B + i\right) + \sin\left(\theta_B - i - \Delta\varphi\right)\right].\cos\gamma}{g} \quad \textit{(Equation 7) .}$$

Table 8 and Table 9 give for each channel the values of λ_e^+ and λ_e^- for some orders. The product of the order and the wavelength at a given pixel, e.g. the central pixel or the two edge pixels, in the "near"-Littrow condition, remains "nearly" constant throughout the complete spectral domain.

It has to be noted that the free spectral range of the NOMAD-channels (*FSR* = 22.56 cm^{-1}) is slightly larger than the spectral span of the detector's sensitive area for lower orders. There the edges of the free spectral range fall off the detector. For orders *m* = 130 and higher, the free spectral range falls entirely on the detector.

Dispersion and Spectral Sampling Interval

Also the spectral sampling interval on the detector is defined by the grating characteristics.

By differentiating Equation 5 we obtain:

$$\frac{g.m}{\cos\gamma}.\partial\lambda = \cos(\theta_B - i - \varphi).\partial\varphi \quad \textit{(Equation 8)} .$$

While wavelength λ_c is forced to fall in the center of the detector, wavelength λ falls a distance D away from the center of the detector:

$$D = f_{imager}.tg\varphi \quad \textit{(Equation 9)},$$

where f_{imager} is the focal length of the imaging system. After differentiation of this equation we have:

$$\partial D = \frac{f_{imager}}{\cos^2\varphi}.\partial\varphi \quad \textit{(Equation 10)} .$$

Combining Equation 8 and Equation 10 the dispersion $\partial\lambda/\partial D$, that indicates how the light is spectrally spread over the detector, can be written as:

$$\frac{\partial\lambda}{\partial D} = \frac{\cos^2\varphi.\cos(\theta_B - i - \varphi).\cos(\gamma)}{f_{imager}.m.g} \quad \textit{(Equation 11).}$$

Table 8. Theoretical values for λ_c, λ_0^+, λ_0^-, λ_e^+, λ_e^-, and the dispersion on the detector at λ_c for SO.

Order	λ_c [μm]	λ_0^+ [μm]	λ_0^- [μm]	λ_e^- [μm]	λ_e^+ [μm]	$\partial\lambda/\partial D$ [cm^{-1}/mm]
100	4.4302	4.4082	4.4524	4.4123	4.4477	1.88
110	4.0275	4.0093	4.0459	4.0112	4.0434	2.07
120	3.6919	3.6765	3.7073	3.6770	3.7064	2.25
130	3.4079	3.3948	3.4210	3.3941	3.4213	2.44
140	3.1661	3.1532	3.1758	3.1517	3.1769	2.63
150	2.9535	2.9437	2.9637	2.9416	2.9651	2.82
160	2.7689	2.7603	2.7776	2.7577	2.7798	3.01
170	2.6060	2.5984	2.6137	2.5955	2.6163	3.19
180	2.4612	2.4544	2.4681	2.4513	2.4709	3.38
190	2.3317	2.3256	2.3379	2.3223	2.3409	3.57
200	2.2151	2.2096	2.2207	2.2062	2.2239	3.76

Table 9. Theoretical values for λ_c, λ_0^+, λ_0^-, λ_e^+, λ_e^-, and the dispersion on the detector at λ_c for LNO.

Order	λ_c [μm]	λ_{0+} [μm]	λ_{0-} [μm]	λ_e^- [μm]	λ_e^+ [μm]	$\partial\lambda/\partial D$ [cm^{-1}/mm]
120	3.6914	3.6761	3.7069	3.6765	3.7059	2.26
130	3.4076	3.3944	3.4206	3.3937	3.4208	2.44
140	3.1641	3.1528	3.1754	3.1513	3.1765	2.63
150	2.9531	2.9433	2.9630	2.9412	2.9647	2.82
160	2.7686	2.7599	2.7772	2.7574	2.7794	3.01
170	2.6057	2.5980	2.6134	2.5952	2.6159	3.20
180	2.4609	2.4541	2.4678	2.4510	2.4706	3.39
190	2.3314	2.3253	2.3376	2.3220	2.3406	3.57
200	2.2148	2.2093	2.2204	2.2059	2.2235	3.76

Table 8 and Table 9 give for both channels the dispersion for the central wavelengths λ_c for some orders, expressed in cm^{-1} per mm. Knowing the width of the detector pixels in the spectral direction, the spectral sampling interval can be easily calculated (see below). The value of the focal length of the imager f_{imager} is a compromise value resulting in the best possible spectral sampling over the complete wavelength range.

Imager Optics

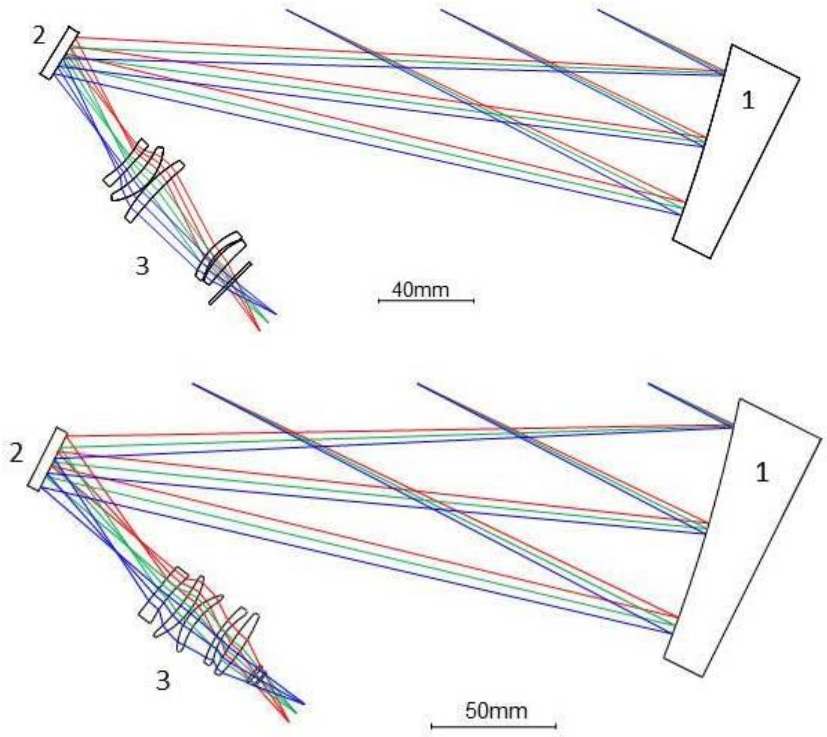

Figure 7. Optical layout of imager (top: SO-channel; bottom: LNO-channel).

The imager optics in NOMAD's infrared channels consists of three elements (see Figure 7): a focusing off-axis parabolic mirror (1), a flat mirror that bends the light path in order to stay within the dimensional constraints of the instrument, and a lens module called detector optics (3). As mentioned earlier, the parabolic mirror has a double use. It serves as collimator for the light that goes towards the grating, and as imager for the light that reflects from it. In both channels this mirror has a focal length of 300 mm and is used off-axis, 19° in SO and 20.75° in LNO. The light is partly reflected out of the horizontal plane, in SO by 1.46°, in LNO by 1.75°. The detector optics image the entrance pupil and the grating on the cold shield of the detector. They project the image formed by the parabolic mirror on the detector with 1X magnification. The lenses used in the module are spherical. To compensate for the aberrations of the parabolic mirror the module is divided in two lens groups that are both tilted and decentered. In SO the lenses are made of Ge, ZnSe, Si, Ge and Si respectively, with clear apertures varying between 20 and 30.5 mm. In LNO the lens materials are Ge, Si, ZnSe, Ge and Si respectively, with clear apertures between 22.1 and 28.2 mm.

Manufacturing and Verification of Gratings

Worldwide only few companies are capable of manufacturing low groove density large area gratings with high enough precision [24]. In Table 7 it is seen that stringent accuracies are imposed on crucial

grating parameters. Especially the accuracy on the groove-to-groove distance (±1 nm) over the total groove height is challenging. This high pitch accuracy is needed to get usable wavefronts, but not easy to achieve due to high tool load and consequent elastic deformations during the ruling process.

Not only the echelle groove pitch needs to be very precise, also the quality (flatness/roughness) of the groove facets is of utmost importance as well as the overall flatness of the grating. Following the DIN3140 standard, the grating surface should have at maximum 0.5 fringes over the total length of the grating (deviation requirement), with at maximum 0.25 fringes difference between two perpendicular directions on the surface (irregularity requirement). Additionally the RMS surface error, measured in reflection, has to be ≤ λ/15, and the slope error ≤ 0.1 mrad. All these requirements are valid at a verification wavelength of 547 nm.

For SOIR on Venus-Express, the American company Bach Research Corporation successfully built such a grating. For NOMAD a manufacturer has been found in Belgium (AMOS).

Contrary to SOIR, the NOMAD gratings and their mechanical support are monolithic, manufactured from one block of 6061-T6 aluminum alloy with hollowed honeycomb back. This results in a non-negligible mass reduction of approximately 20%, it avoids a delicate grating-to-holder gluing process and assures a more homogeneous thermal distribution. The block passed through a double heat treatment for stress relief and stabilization of the substrate, before diamond machining was started. All non-ruled surfaces of the grating underwent a protective chromate passivation conversion (Alodine-1200 coating) while the echelle grooves received first a 20 nm thick Cr transition coating, followed by a final 300 nm thick Au coating (CSL, Belgium).

In order to avoid scattering of light on the adjacent surfaces of the grooves and in the bottom corners (due to rounding by the tip radius *R* of the manufacturing tool), the angle between the reflective surface and the adjacent surface is not 90°, but lowered by a maximum of 6° (Figure 8).

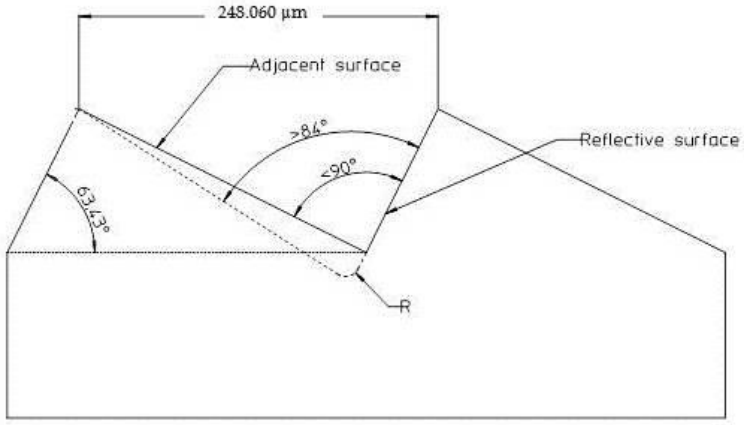

Figure 8. Grating section with slightly over-tilted adjacent surfaces.

For alignment purposes the grating body is foreseen with two mirroring surfaces. Their position has to be known with respect to the reference plane of the grating with an accuracy of 10 arcsec. The mirrors have a reflectivity of ≥70% for visible light and a flatness ≤λ/2 at 632.8 nm.

AMOS produced gratings that, after verification with visible light at 632.8 nm on a laser ZYGO Verifire (for SO) and an RTI 4100 WYKO (for LNO) interferometer through a density pellicle, show full compliance to the surface quality specifications. A comparative test has been performed after delivery of the gratings in order to assess their spectral performance, especially the appearance of unwanted ghost peaks, and their efficiency. The flight spare model of SOIR was used as test setup,

first with a SOIR grating, then with the new NOMAD grating (9). A laser line at 3.39 µm was guided through the system. While on the SOIR grating a clear ghost peak can be distinguished, the NOMAD grating remained free of ghosts. It can also be seen that the NOMAD grating is twice as efficient as the SOIR grating (comparison of the relative main peak intensity). On the other hand the main peak is broader on the NOMAD grating. This last effect can be completely corrected by a detector refocusing.

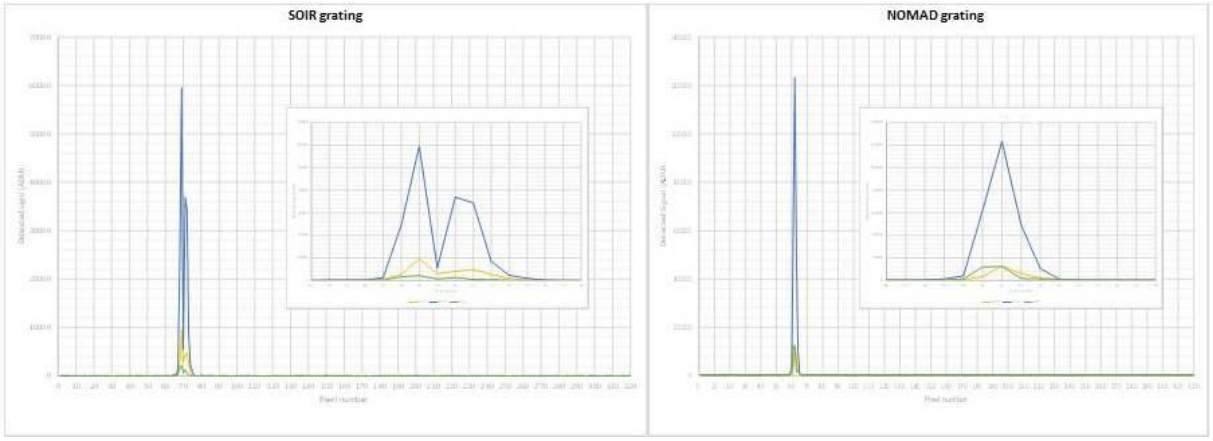

Figure 9. Comparison between SOIR (left) and NOMAD (right) grating.

On samples, representative for the applied Cr-Au-coating, a thermal-vacuum, a humidity, an adhesion and an abrasion test were successfully performed. In Figure 10 pictures of the SO and LNO gratings are shown.

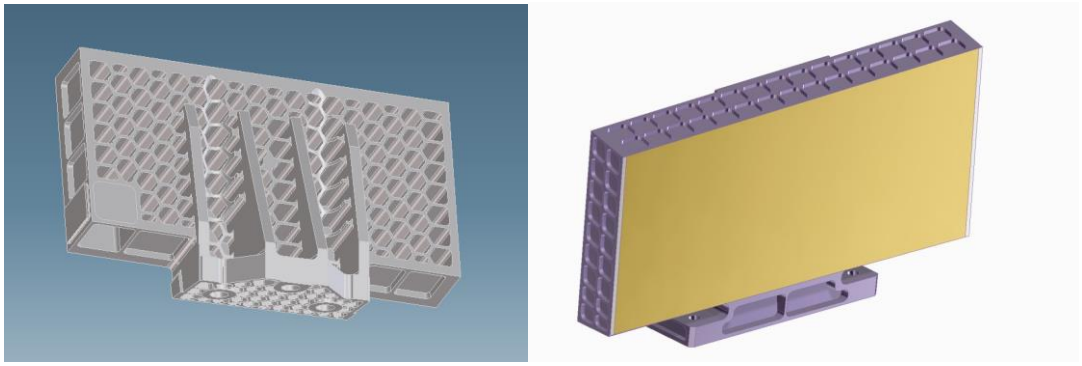

Figure 10. Pictures of SO-grating back (left) and LNO-grating front (right).

Manufacturing and Verification of Parabolic Mirrors

Like the gratings, also the parabolic mirrors are monolithic. They are manufactured by the University of Dundee and provided by Davin Optronics Ltd. (UK). Both the SO and the LNO mirrors have a conical surface with a radius of curvature of 600 ± 0.1 mm, in SO used 100 ± 0.05 mm off-axis and in LNO 109.37 ± 0.05 mm off-axis. In SO the mirror has a clear aperture diameter of 80 mm and in LNO of 103.4 mm. Flat mirror alignment reference surfaces are located on the side and on the back of the parts. The back side of the mirror is hollowed to save mass, but preserves at its contour a full flat back reference surface used during machining. The mirror is rough-manufactured from a block of RSA-6061 aluminum by conventional machining, followed by a thermal treatment for stress relief. The mirror surface, reference mirror surfaces and mechanical interfaces are fine-manufactured by single point diamond turning, ensuring the imposed tolerances (e.g. <1 fringe @ 632.8 nm surface

irregularity and <30 nm RMS surface roughness for the main mirror). The main mirror carries a protective SiO coating with an optical thickness of λ/2 @ 3000 nm. Figure 11 shows the parabolic mirrors for SO and LNO. All dimensions (radius of curvature, off-axis dimension, etc.) plus surface irregularity and roughness have been checked by optical metrology at the Precision Optics Laboratory of Durham University (UK).

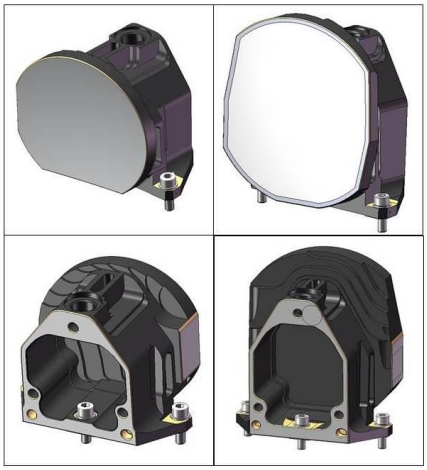

Figure 11. Pictures of parabolic mirror front and rear side (SO left, LNO right).

AOTF Characteristics and AOTF Optics

Working Principle

An important characteristic of acousto-optical tunable filters is that the FWHM of their spectral band, expressed in wavenumber units, is more or less constant over the complete wavelength range with typical values between 22 and 25 cm^{-1}. This means that the passband of the AOTFs can be nicely matched to the free spectral range of the gratings, resulting in an optimized system.

The NOMAD AOTFs are tetragonal crystals made of a birefringent material that is transparent in the applicable infrared domain. The working principle of an AOTF is based on Bragg diffraction [25,26], diffraction that occurs in crystalline structures when an acoustic wave interacts with optical waves. Part of the non-polarized light entering the crystal travels to the exit of the AOTF without diffraction, part is diffracted at a small angle (diffraction angle, see Table 10) with respect to the undiffracted beam. Both the undiffracted and diffracted light beams contain an ordinary and an extra-ordinary polarization component, that exit the AOTF under slightly different angles. The plane of diffraction is the plane formed by the (110)- and (001)-crystal axes (see Figure 12). In NOMAD only the ordinary polarization of the incoming light (k_o) is used. In the AOTF the polarization plane rotates and hence, it is the extra-ordinary polarization of the diffracted light beam (k_e*) that is transferred towards the spectrometer.

The output face of the AOTF is slightly inclined with respect to the input face (angle between input and output plane, see Table 10). This oblique cut refolds the diffracted output beam in line with the optical axis of the channel. The unwanted undiffracted beam is clearly separated from the useful beam (by the diffraction angle) and is easily blocked.

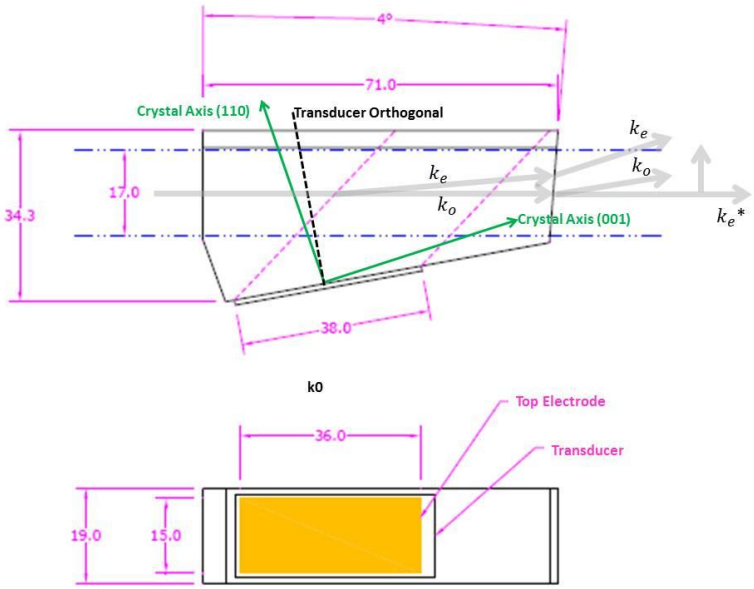

Figure 12. Layout of LNO AOTF with indication of system axes and beam polarization (k_o and k_e are the incoming ordinary and extraordinary beams, k_e is the useful diffracted extraordinary beam).*

Tuning Curve

The acoustic waves, necessary to produce the Bragg diffraction, are injected through a transducer that is glued to a long side face of the crystal. Electrical radio frequent waves are applied to the transducer and converted there in acoustic power. The central wavelength, expressed in wavenumbers, of the AOTF passband is proportional to the applied radio frequency (between 14 and 30 MHz). This relationship is called the AOTF tuning curve. Both the radio frequency and the acoustic power are electrically tunable and hence controlled by NOMAD's central electronics. Examples of AOTF tuning curves are given in Figure 13.

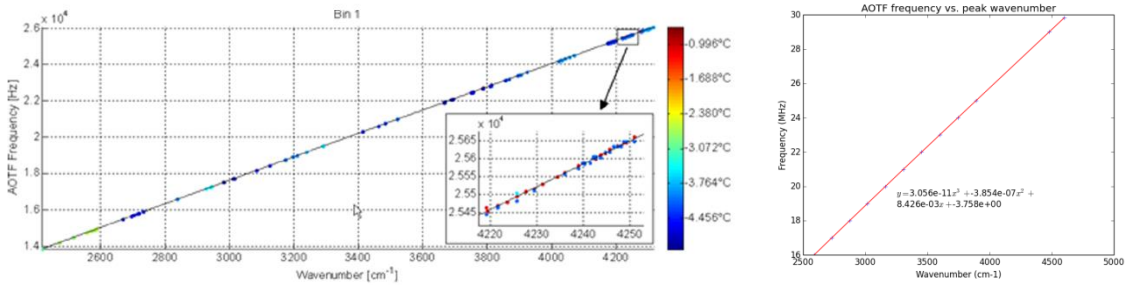

Figure 13. Typical wavenumber to radio frequency tuning curve at a set of working temperatures for the SOIR AOTF (left) and for the NOMAD LNO AOTF at room temperature (right).

It can be seen in the left curve of this figure that the tuning curve is slightly dependent of temperature. This is one of the intrinsic problems of using AOTFs in the infrared wavelength domain. To obtain good diffraction efficiency, non-negligible power (several Watts) has to be used, leading to thermal dissipation inside the crystal. Several mitigation solutions are applied in the design of the NOMAD AOTFs, and especially in the LNO AOTF, where, due to the faint input signal, the highest possible diffraction efficiency is required. One of the solutions is to use an AOTF and transducer that are as long as possible, such that the acousto-optical interaction length is maximized. While for SO the length of the crystal is 50 mm, for LNO a crystal with a length of over 70 mm is used, which is close to the technical limitations of growing pure TeO_2-crystals. Also measures are taken for heat draining from the crystal. The overall NOMAD instrument power budget imposes a maximum allowable RF-power of 2 Watt in the SO and the LNO AOTF.

Side Lobes

When designing AOTFs and their driving electronics, attention should be paid to avoid “pollution” of the main passband through leakage from adjacent orders. In order not to complicate the scientific analysis of spectra, it is important to keep the AOTF’s side lobes as small as possible. For NOMAD a side lobe amplitude suppression of -27 dB is required (4.5% of main lobe), a value that is obtainable by using apodized transducer configurations. Consequently also from electronics point of view it is important to suppress as much as possible the harmonic frequencies of the applied fundamental radio frequency at the output of the RF driver. For NOMAD the suppression is specified to be better than -30 dB (0.001 % of fundamental).

The complete list of specifications for the NOMAD AOTFs is shown in Table 10.

Table 10. AOTF characteristics for the SO- and LNO-channel.

Parameter	SO	LNO	Unit
Material	TeO_2		
Spectral Bandwidth (FWHM)	22 ± 1	24 ± 1	cm^{-1}
Spectral range	2.2 – 4.3	2.2 – 3.9	µm
Acceptance aperture in plane of diffraction	5	17	mm
Acceptance aperture perpendicular to plane of diffraction	5	15	mm
Acceptance angle in plane of diffraction	±3	≥±2.15	°
Acceptance angle perpendicular to plane of diffraction	±3	≥±2.15	°
Diffraction angle	4.2	5.2	°
Diffraction efficiency overall	≥50	≥80	%
Diffraction efficiency @ 3.39 µm	≥60	≥80	%
Distance between input and output plane	50	71	mm
Angle between input and output plane	4.2	4.0	°
Side lobe suppression (absolute)	-27		dB
Side lobe suppression (% of main lobe)	4.5		%
RF frequency	14.20 – 28.00	15.95 – 29.83	MHz
Maximum available RF input power	2		W
Harmonic frequencies suppression (absolute)	-30		dB
Harmonic frequencies suppression (% of fundamental)	0.001		%

AOTF Optics

The SO- and LNO-channels have AOTF entrance and exit optics with differently sized clear apertures, curvatures and focal lengths. The AOTF entrance optics that match the instrument’s entrance aperture (see Table 6) to the acceptance aperture of the AOTF (see Table 10), are telescopes consisting of a Si-Ge doublet lens as objective and a Si singlet as collimator. In SO the magnification of the AOTF entrance telescope is 5X, while in the LNO-channel it is only 1.85X. The AOTF exit optics, that focus the useful beam output by the AOTF onto the spectrometer slit, consists of two ZnSe lenses in the SO-channel, and of a Ge-Si-doublet in the LNO-channel.

Manufacturing and Verification

The NOMAD AOTFs are paratellurite (TeO_2) crystals, custom manufactured under the responsibility of Gooch and Housego, UK. For the delicate operation of mounting the transducers to the AOTF crystals, this company applies specific materials (e.g. the glue to fix the transducer to the crystal) and follows propriety procedures (e.g. thickness of the glue layer). Each crystal-transducer combination gets a hand tuned matching network aiming to get the input impedance as close as possible to 50 Ω. Gooch and Housego own patents on apodization of transducers for side lobe suppression.

For protection reasons the AOTFs with their matching network are placed in an aluminum box with an entrance and exit aperture. To limit the influence of temperature on the optical properties of the AOTF, it is important that the power dissipated in the crystal is efficiently drained away. For the smaller SO-crystal a bottom heat drain is foreseen in AISI 316 stainless steel, a material with a thermal expansion coefficient close to the one of TeO_2. For the bigger LNO-crystal heat evacuation is foreseen from top and bottom (Figure 14).

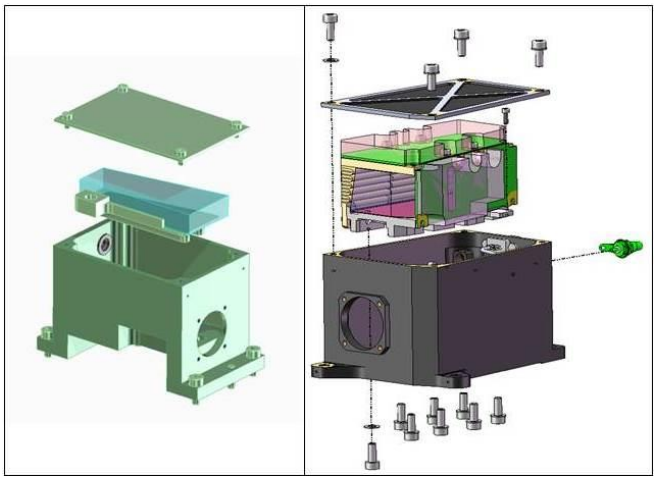

Figure 14. Pictures of NOMAD AOTFs (SO left, LNO right).

An extensive set of acceptance tests has been performed after delivery of the crystals. One of the most important features to be verified is the side lobe suppression. This is performed by illuminating the entire aperture of the AOTF homogenously with HeNe laser light (3.39 µm). The AOTF is mounted on a rotation-and-translation stage that is translated until the laser beam is centered in the entrance aperture and rotated until the diffracted peak falls on a PbSe detector, itself sitting on an independent rotation stage. The AOTF radio frequency is scanned up and down from the central frequency in small steps. Figure 15 gives, both on a linear and a logarithmic scale, the response curve (normalized diffracted intensity versus radio frequency) for the LNO AOTF. It is noted that side lobes stay nicely below the specified value of 4.5 %.

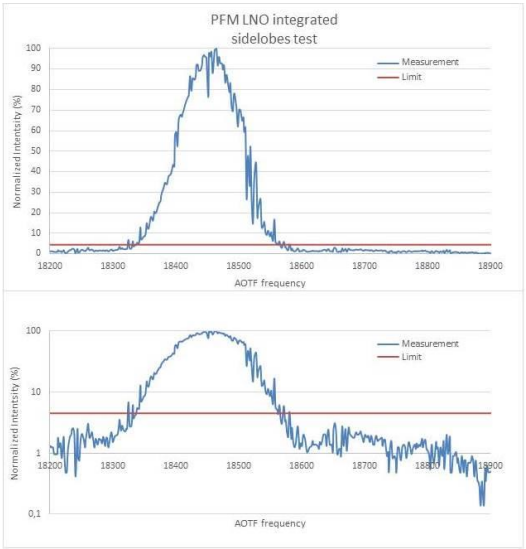

Figure 15. Normalized response curve of the LNO AOTF as a function of radio frequency (top: linear, bottom : logarithmic, red line: limit specification of 4.5%).

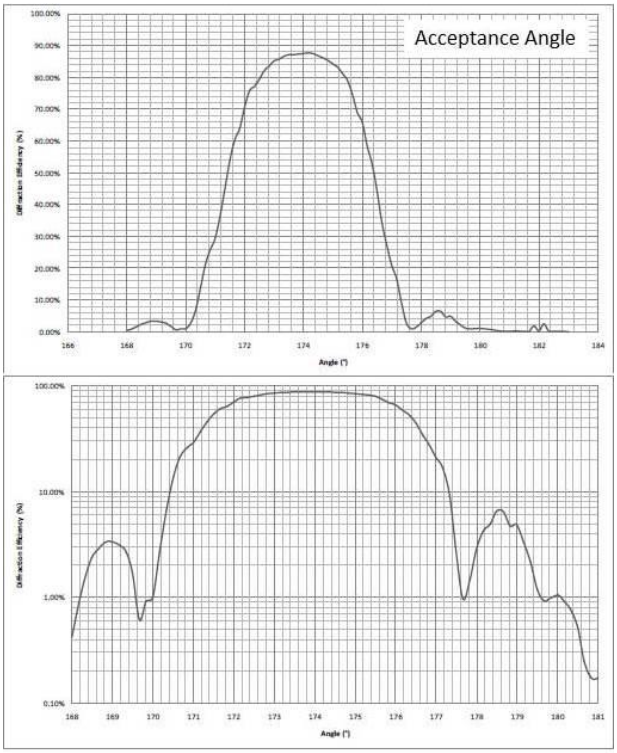

Figure 16. Acceptance angle of the SO AOTF (top: linear, bottom : logarithmic).

To test the dependence of diffraction efficiency on RF input power, the AOTF is positioned and the RF frequency tuned such that the main diffracted peak falls on the detector. By scanning through the power range from 0 to 2 W (maximum allowable input power) it is seen that for the SO AOTF the specification on the diffraction efficiency (≥60%) is met with a value of around 86% for an input power of 1.8 W. For the LNO AOTF the requested diffraction efficiency of ≥80% is met for much higher RF power values (around 8 W). In NOMAD only a maximum of 2 W will be injected into the AOTF, resulting in a sub-optimal diffraction efficiency in LNO of about 62% at 2 W. By performing an angular step-scanning of the detector rotation stage with respect to the AOTF, also the angle between the undiffracted and diffracted beams is verified. The acceptance angle of the AOTFs is measured by locking the detector again on the diffracted peak, but now performing an angular step-scanning with the AOTF rotation stage (the laser light enters the AOTF under different angles). Figure 16 shows the acceptance angle in the plane of diffraction of the SO AOTF, both on a linear and logarithmic scale. The measured acceptance angle FWHM is ±2.6°, a bit smaller than the required ±3°.

The uniformity of the diffraction efficiency over the entrance aperture of the AOTF is verified by locking the detector and AOTF rotation stages to the diffracted peak, whilst performing a horizontal and vertical linear step-scanning with the translation stage .

Finally also the Voltage Standing Wave Ratio (VSWR) is registered for each AOTF. While the theoretical input impedance of the AOTF system is expected to be 50 Ω, in reality it is dependent on the applied frequency. The VSWR gives an indication about the degree of input impedance mismatching. The further the VSWR deviates from 1, the more power will be reflected back from the AOTF. The knowledge of the frequency-to-VSWR relationship of the AOTF is a necessary input for the design of the electronic RF-driver. It should not exceed a value of 3. Figure 17 gives the VSWR-curve for the SO AOTF.

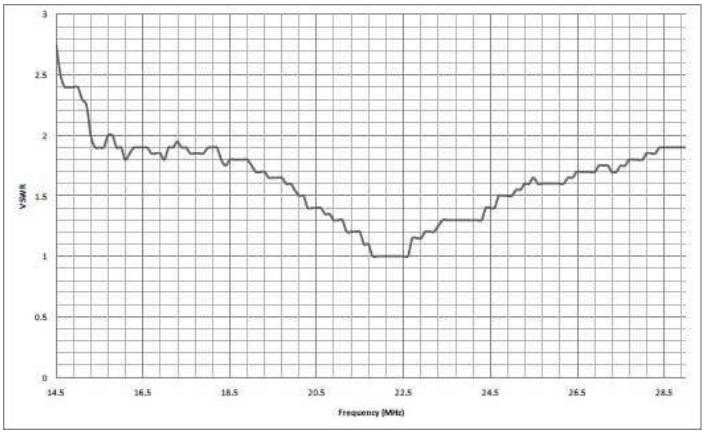

Figure 17. Voltage Standing Wave Ratio (VSWR) of the SO AOTF.

Field of View and Beam Shaping

The Spectrometer Slit

The field of view of the SO and LNO-channels is fixed by the dimensions of their spectrometer slits. It is explained above how the science requirements led to a slit of 2'x30' in SO. Following the Nyquist sampling criterion, it is good design practice to sample the instrumental line profile (2') by at least 2 detector pixels. The dimensions of the pixels in the selected NOMAD detectors (see below) are 30 x 30 μm^2. Therefore the size of the slit in SO is 60 x 900 μm^2. To have the same performance in the LNO-channel when used in solar occultation mode, at least the part of the slit that is illuminated by the Sun (24') should have been only 2' wide too. To optimize the SNR we have opted for a slit that is 4' wide over its entire length. This results in an SNR that is more than 10% larger compared to the SNR with a slit that has a narrow central part. Increasing also the height of the LNO slit as much as possible in order to increase signal during nadir measurements, its size was fixed to 4' x 150' or 120 µm x 4.5 mm. To reduce the smile (see also below) of such a high slit on the detector, it is curved (radius of curvature = 72.5 mm)(see Figure 18). The *sag* over the central part of the slit that is illuminated by the Sun (24' or 720 µm) , is less than 1/30th of a pixel and will therefore not be noticed when performing solar occultation measurements.

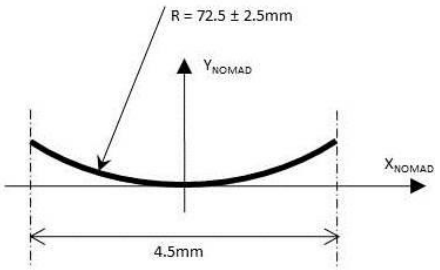

Figure 18. Curvature of LNO slit (exaggerated representation).

Diaphragms at the Entrance Pupil

A diaphragm is placed at the location of the entrance pupil, just in front of the first lens of each of the channels. In SO, where the f/# of the optics is limited by the entrance pupil, the main purpose of this diaphragm is to better match the footprint of the beam on the grating to the physical size of the

grating. This is at the expense of a small loss in light flux of 4%. In LNO the f/# is limited by the cold shield. The diaphragm placed at the entrance pupil is slightly larger than the image of the cold shield and serves to minimize the amount of stray light entering the instrument. In Figure 19 the shape and dimensions of the SO and LNO diaphragm are given. For SO the resulting footprint on the grating, and for LNO the footprints of the beams limited by the cold shield are also shown.

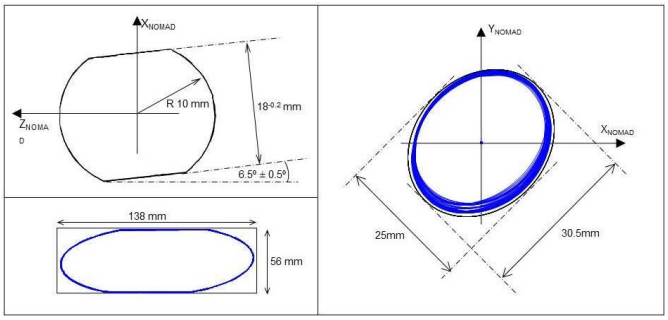

Figure 19. Diaphragm at the entrance pupil for SO (top left) and footprint of beam on the grating (bottom left). Diaphragm at the entrance pupil for LNO and footprints of beam limited by cold shield (right).

Diaphragms in the AOTF Entrance Optics

The initial purpose of a diaphragm in the entrance optics of the SO AOTF (situated between the objective and the collimator lens sets) was to block superfluous Sun light from entering the instrument. In SOIR at Venus, closer to the Sun, some 70% of the light was blocked. In NOMAD at Mars the image of the Sun on the diaphragm will be approximately half in size, rendering its blocking functionality more or less useless. The diaphragm has not been completely removed however. It has been enlarged, but such that it still maintains its secondary function, i.e. to prevent that zero-order light from an out-of-field straylight source, entering the AOTF under a critical angle, would be able to reach the spectrometer slit. In the LNO-channel during nadir observations, where the signal will be approximately 10^6 times lower than the signal from the Sun, it is even more vital that zero order light cannot pass the AOTF and reach the spectrometer slit and hence to use a narrow enough diaphragm.

Detectors and Read-out Electronics

Detectors and Coolers

As described above, the parabolic mirror forms an image of the spectrometer slit and projects it on the detector's sensitive area with a magnification of 1. The position of the detector is inclined so that its optical axis coincides with the optical axis of the imager optics and to bring its pixel columns in line with the image of the spectral lines produced by the grating.

The detector used in NOMAD is the standard MARS-MW K508HSM Integrated Detector Dewar Cooler Assembly (IDDCA) manufactured by Sofradir, France. This MARS-MW detector is a photovoltaic mercury cadmium telluride (MCT) detector with a focal plane array (FPA) of 320 columns by 256 rows and 30 x 30 μm^2 sized pixels. The FPA is lodged in a vacuum dewar with a customized 1 mm thick silica front window (refractive index n = 3.4) with anti-reflective coating. In the dewar a cold radiation shield with an f/3.936 aperture shields the FPA thermally from its surroundings. The aperture of the cold shield is precisely aligned with the detector pixels. The FPA is cooled down by a K508HSM rotative Stirling cooler (manufactured by Ricor, Israel). The off the shelve version of this detector is modified for the NOMAD application. It has a different cooler body and the integrated cooler motor

control circuit has been discarded and replaced by an external space qualified design of BIRA-IASB. But the most important adaptation is the customization of the wavelength range. The material of the dewar window (Si) defines the cut-on wavelength (around 2 µm at 50% of maximum response). The MCT composition of the FPA defines the cut-off wavelength. This is true for the SO-detector (around 4.2 µm at 50% of maximum response). In LNO however a 0.3 mm thick germanium cold filter (refractive index n = 4) is added on top of the cold shield, cutting short the wavelength range (cut-off wavelength around 3.9 µm at 50% of maximum response). In Figure 20 the normalized spectral responses of the SO and LNO detectors are shown.

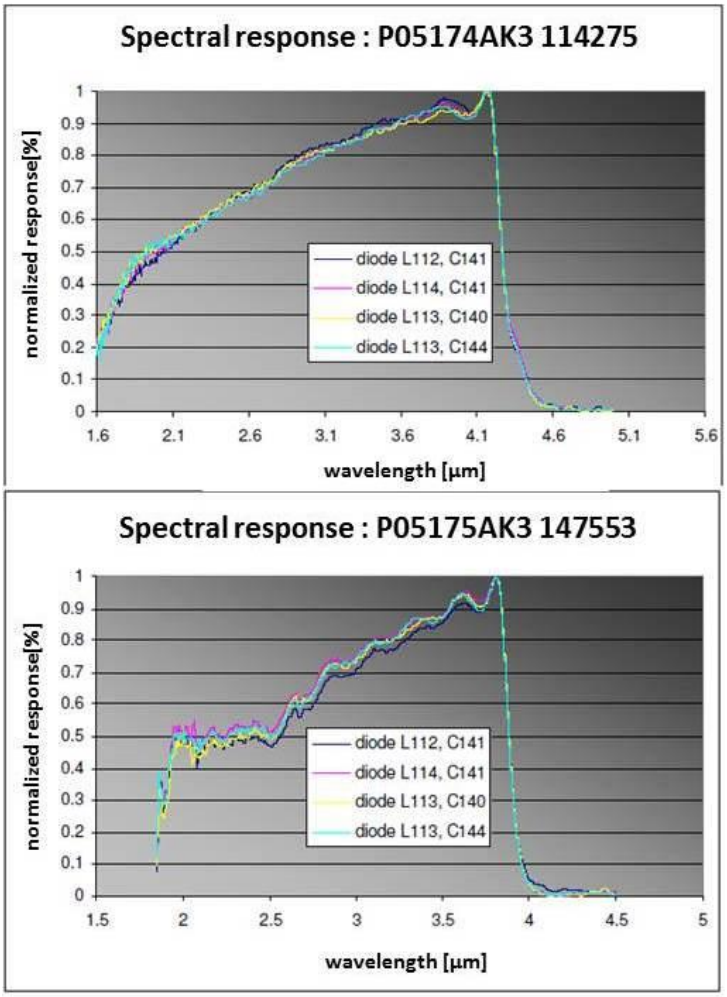

Figure 20. Normalized spectral response of detectors (SO: top, LNO: bottom).

In SOIR on Venus-Express a K508 cooler from Ricor was used. This cooler has a declared life time (MTTF) of ≥8,000 hours, which is sufficient for solar occultation missions (SOIR, NOMAD SO-channel) but not for nadir missions (NOMAD LNO-channel). A solution offering a significant increase in MTTF was proposed for NOMAD with Ricor's K508HSM, a derived product from K508 with modified stator coil windings allowing a lower operating pressure and, hence, reduced pressure on the compressor's ball bearings. The expected MTTF for the H508HSM is ≥12,000 hours.

This detector-cooler assembly is extensively described in literature [27]. An overview of the rest of its characteristics is given in Table 11.

Table 11. Detector and cooler characteristics for the SO- and LNO-channel.

Parameter	SO	LNO	Unit
Number of pixels per column	256		
Number of pixels per row	320		
Pixel size	30 x 30		μm^2
Cold shield aperture (*f/#*)	f/3.936		
Integration capacitor (gain 0 / gain 1)	0.7 / 2.1		pF
Maximum charge (gain 0 / gain 1)	12.0 / 37.0		10^6 e^-
Video output range	1.6 – 4.4		V
Video dynamic range	2.8		V
Minimum integration time	3		µs
Wavelength range (50% of response)	2.0 – 4.2	2.0 – 3.9	µm
Typical quantum efficiency at 3.5 µm	0.75		e^-/photon
Linearity (charge 7 to 97% of pixel saturation)	95		%
Read-out speed for single video output	1		MHz
Typical focal plane temperature	90		K
Cool down power consumption (273 to 90 K)	10.6		W
Regulated temperature power consumption (at 90 K)	3.8	3.5	W
Cool-down time (273 to 90 K)	261	266	s

Read-out Electronics

When an IR photon with wavelength below the cut-off impinges on the MCT sensitive area, it creates an electron-hole pair that is immediately separated by the internal electrical field of a photovoltaic diode. The 320 x 256 photovoltaic diodes (pixels) are individually coupled by indium bump technology to a raster of charge capacitors laid out on a CMOS read-out integrated circuit (ROIC) at the back of the FPA. For the duration of the programmed integration time, the capacitors are fed with the electrons from the photovoltaic diodes by direct injection and store the charge. At the end of the integration process all the charges are converted to voltages and multiplexed into an analog video signal at the output of the ROIC. A consequence of using the direct injection method is that the linearity of the read-out is not guaranteed for low signals and for signals close to saturation (see Table 11). It is important to note that this type of detectors has a windowing mode, allowing to read-out only a reduced window of detector pixels.

Using the FPA at temperatures above 130 K could harm the detector. Therefore two diodes are integrated in the FPA and used as temperature sensors (injecting a constant current, then measuring the voltage over the diode that is proportional to the temperature). They allow the control loop to verify if the requested cold FPA temperature setting (typically around 90 K) is reached.

System Control Electronics, Firmware and Software

Channel Electronics

Both the SO and the LNO-channel have a completely separate dedicated space qualified electronic control unit (Figure 21). In this unit one can distinguish three chains, one for each of the three electronically driven devices: the AOTF, the FPA and the cooler. The three chains are controlled from a central control and communication board (CCC) that is built around a Xilinx field programmable gate array (FPGA). For the AOTF chain, a direct digital synthesizer (DDS) is implemented inside the FPGA that produces a code that represents digitally the radio frequency sine waveform that has to be applied to the AOTF. This code is transformed in an analog signal on the radio frequency generator board (RFG). This low power RFG-signal is then amplified in a radio frequency power amplifier, the

design and manufacture of which has been subcontracted to a specialized company (ERZIA, Spain). Finally the amplified RF-signal is applied to the AOTF's matching network and transducer.

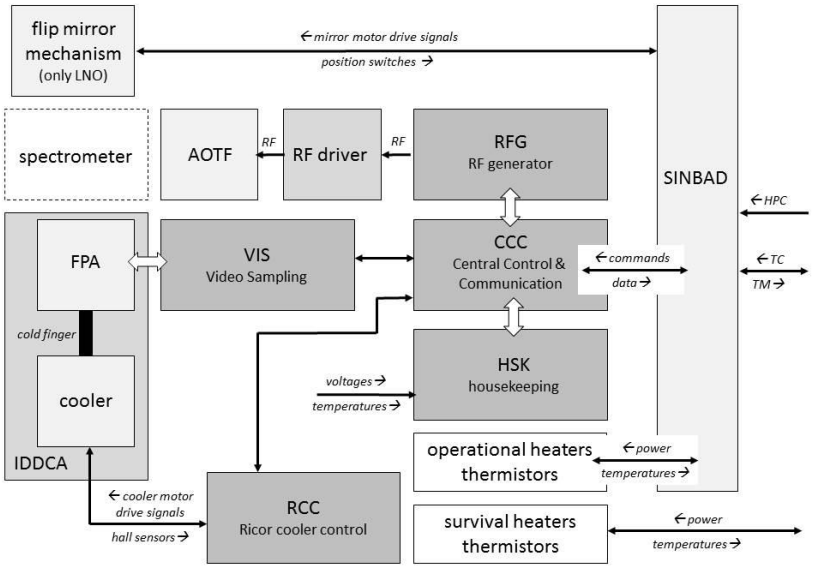

Figure 21. Block diagram of electronics of SO and LNO-channel.

Table 12. Characteristics of the SO RF power amplifier

Characteristic	Value or Range	Unit
RF frequency band	14.2 - 28	MHz
Maximum RF input power (@ 14 MHz)	2.16	dBm
Maximum RF input power (@ 28 MHz)	0.73	dBm
Input impedance	50	Ω
Maximum RF output power	33	dBm
	2	W
RF output settling time	<1	ms
Unwanted spectral components e.g. harmonics	<-20	dBc
Efficiency at maximum RF output	33	%
Nominal load (AOTF impedance)	50	Ω
Acceptable AOTF VSWR	1 - 3	
Supply voltage	11.82 – 12.18	V
Maximum allowed DC power consumption	6	W

The design of the radio frequency power amplifier focused on spectral quality. Since the power amplifier frequency range covers approximately one octave, it is important that the second harmonic of the generated carrier is suppressed as much as possible (≤-30 dBc). A customized amplifier design was implemented and an extra sharp low pass output filter added to remove any remaining unwanted spectral components. Low DC power consumption (≤6 W) was set out as a critical requirement because of the limited DC power resources in NOMAD. In the power amplifier design physical properties were taken into account, such as input impedance, voltage standing wave ratio (Figure 17) and RF input power, all as a function of wavelength, of the real AOTFs. Also the diffraction efficiency of the AOTFs as a function of AOTF input power was a driver during design.

Table 12 gives an overview of the characteristics of the power amplifier. Figure 22 shows the 2nd and 3th harmonics levels for the SO-channel power amplifier. It is clearly seen that the initial requirement of harmonic suppression under -30 dBc could not be met. Figure 23 shows that the DC power of the

amplifier is successfully kept below the specified value over the complete wavelength range and for different amplifier RF output power levels.

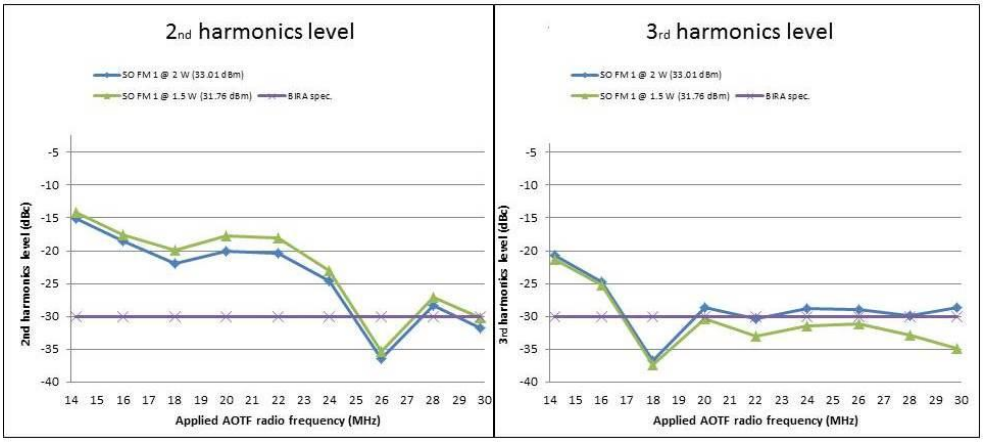

Figure 22. Second (left) and third (right) harmonics levels of the radio frequency power amplifier (SO).

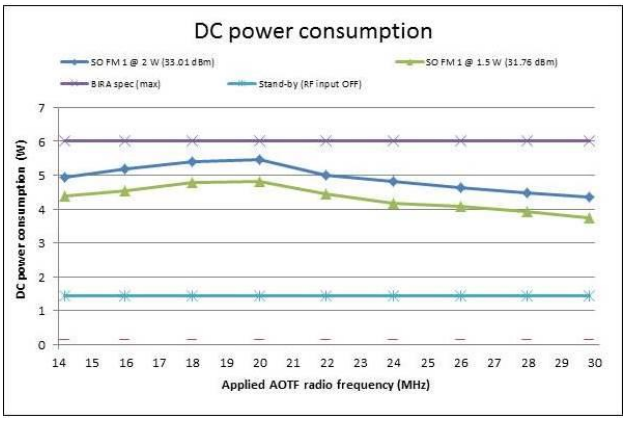

Figure 23. DC power of the radio frequency power amplifier (SO).

A second chain in the channel electronics concerns the detector. The FPGA on the CCC board generates the clock signals and other parameter settings (gain, window mode) needed to read out the FPA. The analog video signal from the detector (see above) is sampled on the VIS board, amplified, converted to digital and transferred to the CCC board.

The third chain is used to drive the cooler. The FPGA sends a digital control signal, representative for the desired motor speed, to a digital-to-analog convertor on the RCC board. The resulting analog signal is used as input to a motor controller hybrid that generates pulse width modulated phase signals to drive the brushless 3-phase DC motor of the cooler. Three hall sensors detect the position of the motor rotor and are fed back to the motor controller.

Besides the three main chains, the channel electronics also contains a HSK board that collects measurements from temperature, voltage and current sensors, digitalizes them and returns them over multiplexers to the FPGA on the CCC board.

Front Line Power and Control Unit (SINBAD)

The electrical interface between the NOMAD instrument and the spacecraft is not situated in the channels themselves. The SO, LNO and UVIS electronics interface to NOMAD's front line power and control unit (SINBAD). SINBAD can be switched on and off by the spacecraft through high power

commands. While on, it is powered by an unregulated voltage and can interact with the spacecraft through a MIL-standard 1553 bus (uploading telecommands, downloading housekeeping data) and a SpaceWire link (downloading science data). SINBAD switches on and off each of the three NOMAD channels depending on the imposed observation timeline (see below). It regulates the primary power and offers a stable voltage to the channels. SINBAD is built around two Actel FPGA's. The primary FPGA (Shireen) contains a firmware LEON3 microprocessor running a real time operating system (RTEMS) to which a series of software management functions are added, amongst which a telecommand interpreter and a file operation management system allowing versatile use of the available on-board memory. The secondary FPGA (Chimera) controls the flip mirror mechanism (only in LNO) and NOMAD's operational heaters and thermistors (see below), but has to be seen primarily as a firmware extension of the SO and LNO-channels. Chimera streamlines the registration of spectra in these channels by sending them in a timely manner command packets and by capturing in memory, at high speed, the data stream they send back on the fly.

During ground testing, the instrument can be operated from a dedicated electrical ground support equipment, running a user friendly software interface developed in Python.

Observation Sequence and Modes

The science operations during one orbit around Mars can be split in four distinct observations. At day side NOMAD will perform nadir observations with the LNO and UVIS-channels. At the sunset terminator a solar occultation measurement will be performed with the SO and UVIS-channels. At night side again nadir measurements can be done with LNO and UVIS. At the sunrise terminator a solar occultation measurement will be performed with SO and UVIS. Thanks to the presence of the flip mirror in LNO, it is also possible to use LNO instead of SO during solar occultations. Using SO and LNO at the same time is excluded though due to spacecraft power limitations.

Just before starting a nadir observation or solar occultation measurement with one of the infrared channels it is necessary to cool the detector down to its operating temperature of approximately 90 K. A command packet is sent to the channel to start this precooling phase. This packet contains parameters such as the cooler temperature set point, an open or closed loop flag and some cooler coefficients allowing smooth regulation. During precooling (duration is maximum 600 s, depending on the temperature of the environment) no spectra are recorded, only housekeeping is sent every second. At the end of the precooling phase, the channel starts a science observation upon reception of a new command packet. This time the command contains parameters that will permit the channel to do 'real' measurements, such as the AOTF frequency and AOTF power set points, the detector integration time, window frame dimensions, the binning factor, and more. For nadir, longer integration times are anticipated and therefore the typical sampling time is 15 s. During solar occultations integration times will be much shorter and the sampling time is 1 s.

The on-board software of the channels offers a wide range of features to tailor the measurements to the scientific needs. During one measurement, i.e. in the time frame of 1 second (solar occultation) or 15 seconds (nadir) it is possible to perform up to 6 consecutive measurements, each with different parameter settings. In this so called hopping mode it is e.g. possible to measure in 6 randomly chosen spectral domains (6 AOTF frequency settings corresponding to 6 grating orders). It could be an option to dedicate one of the 'domains' to a dark measurement with the AOTF switched off. Moreover, it is possible to switch from a set of 6 initial subdomains (used during the first half of the observation) to

6 totally different subdomains in the second half. This is especially useful during solar occultation where the science interest in the upper atmosphere can be quite different from that in the lower atmosphere.

Accumulation is a technique that, inside one subdomain measurement, allows to increase the SNR of the measurement by adding a series of consecutively registered spectra. The recording of a spectrum, i.e. the frame that is read-out from the detector after one integration time slice, could be repeated a number of times and added in memory to the accumulated pixel-by-pixel sum of the previous ones. While the subdomains have to fit within the time frame of one measurement (1 and 15 seconds for SO and LNO respectively), the combination of integration time and number of accumulations has to fit within the duration of one subdomain measurement. Figure 24 shows an example of a NOMAD observation sequence for one orbit.

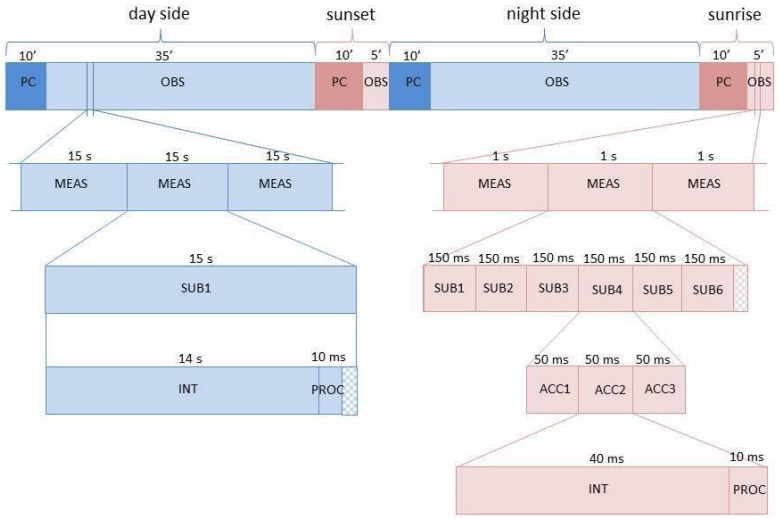

Figure 24. NOMAD observation sequence. PC = precooling; OBS = observation (nadir or solar occultation); MEAS = measurement; SUB = subdomain; ACC = accumulation; INT = integration time; PROC = process time (including detector read-out, AOTF settling, ...). Left (blue): nadir observation with 1 subdomain, no accumulation, spectra with 14 s integration time. Right (red): solar occultation observation with 6 subdomain, 3 accumulations in subdomain 4, spectra with 40 ms integration time.

When composing commands for the SO and LNO-channels it is important that the time combination of integration times, processing times, number of accumulations and number of subdomains stays within the sampling time. Besides a hopping mode, NOMAD can be commanded in stepping mode, meaning that from one measurement to the next a parameter (e.g. frequency, integration time, window top, ...) is incremented by a step value. The stepping mode can be handy during on-ground or in-flight calibration of the channels, when e.g. the full detector window has to be read or a frequency scan over the whole spectral domain has to be performed. NOMAD calibration will be reported upon in a separate publication [28].

For each recorded spectrum, all illuminated detector lines are read-out by the channel electronics, i.e. 24 lines in the SO-channel and the LNO-channel when working in solar occultation mode, and 144 lines in the LNO-channel when working in nadir mode. However, due to data rate limitations at spacecraft side, during one sampling time only the equivalent of 24 detector lines can be processed by the spacecraft and transmitted to Earth. This has a number of consequences on NOMAD's observation philosophy. First of all, this means that in LNO the 144 read lines will be always reduced to 24 'super-lines' through binning by 6. If a measurement consists of only one subdomain the 24

read (super)lines will all be transmitted to Earth. If a higher number of subdomains is used per measurement, a corresponding line binning will be applied. For the red example of Figure 24, where a measurement consists of 6 subdomains, binning by 6 will be applied to the lines, and only 4 'super-lines' will be processed per subdomain. Binning of lines has an impact on the spatial resolution of the channel.

The severe limitation in allowable number of payload telecommands during this ExoMars mission (≤10 telecommands per orbit for NOMAD) has resulted in the implementation of on-board channel observation parameter (COP) tables with a nearly unlimited number of preprogrammed combinations of instrumental parameters. If modifications still appear to be necessary, these tables can be patched from ground.

Mechanical Structure, Structural Analysis and Alignment

Mechanical Structure

NOMAD is housed in an aluminum structure, consisting of two base plates, the bottom one serving as optical bench for the SO-channel, the top one for the LNO-channel. A set of carrier walls interconnects the SO and LNO base plates. The base plates are flat topped but have a ribbed structure at the bottom in order to reduce weight but maintain strength and stiffness. The useful surfaces are 428 x 306 mm^2 for the SO optical bench and 439 x 316 mm^2 for the LNO bench. On the SO base plate an area is kept free where the UVIS-channel, that sits on its own intermediate base plate, can be inserted. The thickness of the SO plate is 90 mm and of the LNO plate 56.8 mm. The SO base plate is thicker because it has a box shape, open at the bottom, that is used to lodge SINBAD and the electronic units of the SO and LNO-channels. Figure 25 and Figure 26 show 3D drawings of the SO and LNO base plate. The important mechanical elements can be recognized in each channel: a solar occultation periscope carrying the entrance mirrors, an AOTF bridge carrying the AOTF box and the AOTF entrance and exit optics, the support of the grating (milled from one block together with the optical part), the support of the parabolic mirror (milled from one block together with the optical part), some optical mounts (for spectrometer slit, folding mirror, imaging optics) and the foot for the detector-cooler assembly. Only two electronic modules, each in their mechanical box, are present on the optical bench: the VIS board (close to the detector) and the RF power amplifier (close to the AOTF). The walls of LNO and the top cover do not serve any structural goal. Together with the SO walls, they are merely used as support structure for the multilayer insulation (MLI) that encloses the whole of NOMAD (see below). The complete +Z-side wall of NOMAD and a small part of the top cover (+X-side) are manufactured in one piece and serve as radiator (see below), as it is directed towards deep space in most phases of the mission.

In the electronic section, at the bottom of the SO base plate, all the electronic boards are protected by individual mechanical boxes. From this section the harness, that is manufactured by Glenair, UK, is routed up to the three channels.

Nearly all mechanical parts are made in 7075-T7351 thermally pre-treated aluminum. For better manufacturability some optical parts are made from 6061-T6 aluminum (gratings, flip mirror) or RSA-6061 aluminum (parabolic mirrors). Most of the mechanical elements, and especially those close to the optical path, have undergone a space qualified optically black anodization (Protection des Métaux, France). This should limit scattering of light and keep the influence of thermal background as

low as possible. Contact surfaces between mechanical parts are kept free of anodization but have been treated with alodine 1200 for good electrical conductivity. In order to achieve good thermal contact between base plates, walls and optical mounts, mechanical provisions are foreseen in the contact planes where thermal filler can be placed. The outside of the radiator part has been painted white (see below).

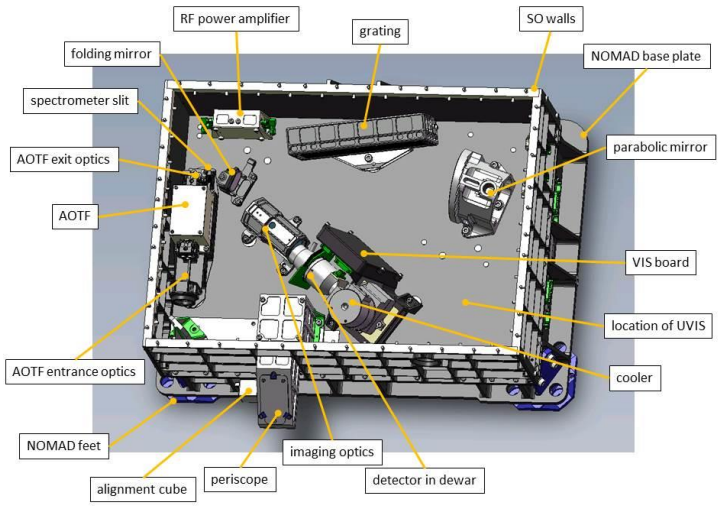

Figure 25. 3D view of the SO-channel.

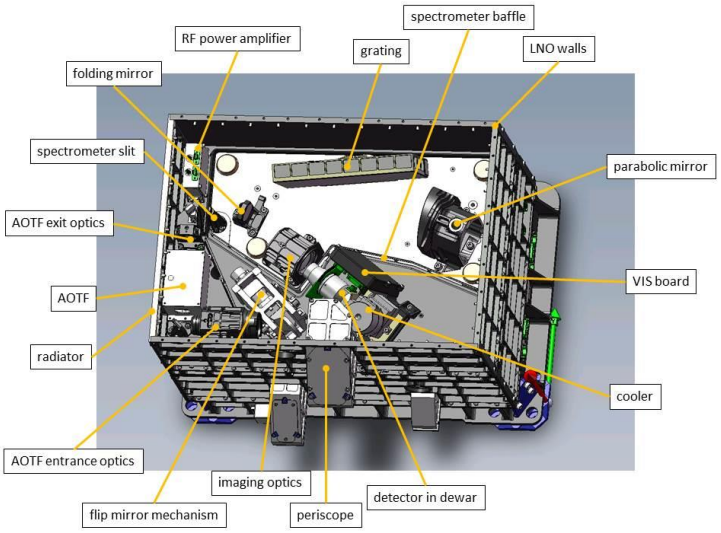

Figure 26. 3D view of the LNO-channel.

The most noticeable exceptions to the all-aluminum approach are the three NOMAD feet that form the mechanical interface to the spacecraft. In order to insure the thermo-mechanical stability of the spacecraft instrument deck, a very low thermal conductance is imposed between instrument and spacecraft. Therefore the feet are made from titanium, that has a ten times lower thermal conductivity than aluminum, and contain a double intrinsic thermal barrier, one in the mounting plane to the spacecraft (3 x M8 screws) and one at the interface of the feet with the instrument (4 x M5 screws). Despite the dedicated mechanical design a non-compliance is reported on the thermal conductance between NOMAD and the spacecraft (see below). The three feet have crumple zones

giving them sufficient elasticity to act together as isostatic mount for the instrument, limiting the transfer of elastic deformation from spacecraft deck to instrument and vice versa.

Structural Analysis

A very detailed structural analysis was performed using a finite elements mathematical model (SMM) (MSC NASTRAN 2010) based on the CAD model of the instrument. The stiffness has been verified by normal mode analysis. Eigenfrequencies are calculated for the 3 translational and the 3 rotational degrees of freedom, each with its associated modal effective mass (MEM). In Figure 27 it can be seen that the requirement of a first overall eigenfrequency of the instrument ≥140 Hz is not met.

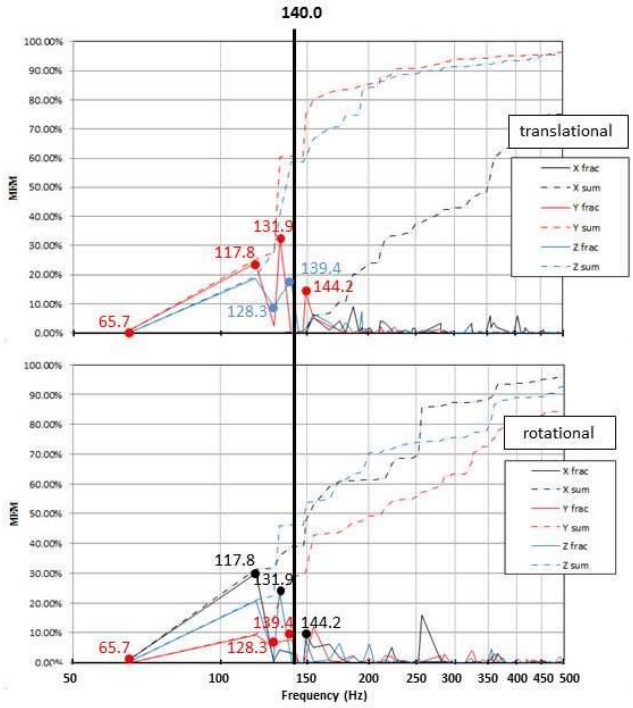

Figure 27. Normal mode analysis result : modal effective mass (MEM) as a function of frequency. Six first eigenfrequencies are indicated with dots. Continuous line is fractional MEM, dotted line is summed MEM. Top: translational degrees of freedom. Bottom: rotational degrees of freedom.

Two modes (117.8 Hz and 131.9 Hz) are found below this limit with non-negligible MEM. Further a quasi-static load analysis was performed on the interface bolts for load cases along different directions. The results show no surpassing of the maximum allowable load on the deck inserts (2046 N axial, 1665 N in mounting plane). Also a stress analysis was done on the titanium interface feet showing that, although stress is highest in the regions of the bolt holes and the elasticity 'hinges', the modelled values are below the stress limit values for titanium. Finally, in preparation of later vibration tests on the 'real' instrument, loads have been simulated for sine and random vibrations.

Qualification level vibration and shock tests were run successfully (CSL, Belgium and IABG, Germany) on the so called structural thermal model (STM) of the instrument, a model that is completely representative for the flight model as to what mass, center of gravity and moments of inertia are concerned. The test results obtained on the STM have been correlated with the mathematical model predictions. The tests were repeated with acceptance level loads on the proto flight model (PFM).

Flip Mirror Mechanism

A movable mirror, the so called flip mirror, selects, as input for the LNO-channel, either the light beam from the nadir or from the solar entrance. The nadir and solar positions of the mirror correspond to the two end positions of the mechanism carrying the mirror. The nominal position of the flip mirror is 'nadir'. During launch the flip mirror will be placed in an intermediate position offering the best resistance to vibrations. While in the 'solar' position the only constraint is that the mirror is completely out of the beam, in 'nadir' some in-beam position accuracy is required (±5 mrad). The mirror is mechanically aligned such that it makes an angle of exactly 45° with the optical axis, fulfilling the accuracy requirement. The movement of the mirror in the reflection plane however does not guarantee this accuracy, reason why its surface is slightly oversized. A stepper motor-demultiplicator system (Thales Alenia Space, France), that is suspended in an aluminum cradle-in-cradle structure, drives the mirror through a worm-worm wheel gear. In normal operation the cradles are kept solidary by means of a pin, but in case of a motor failure, the pin can be retracted (pin puller), so that a spring-assisted separation of the cradles will take place and the mirror will be forced definitely in its fail safe position (= 'nadir' position). In the two end positions a nominal and redundant position switch are mounted and a hard stop. Figure 28 is a 3D drawing of the flip mirror mechanism.

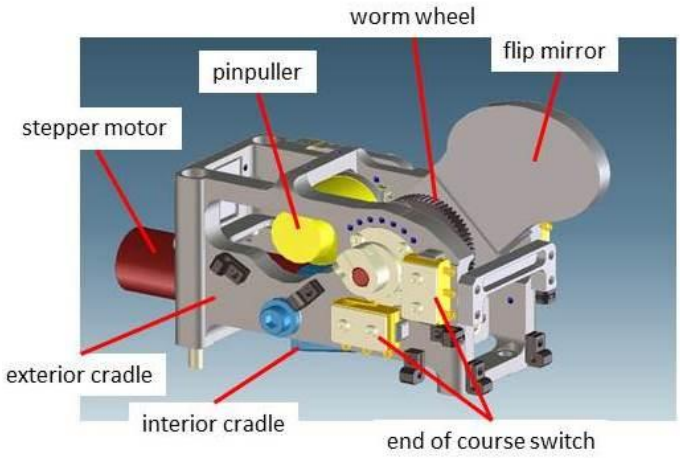

Figure 28. Flip mirror mechanism.

Optical Co-alignment

The NOMAD instrument has three periscopes protruding from the –Y-face of its main volume, one in each of the channels, allowing them to perform solar occultation measurements at the Martian limb (67.07° off the nadir direction). While the optical co-alignment of the nadir lines of sight is driven solely by the mechanical tolerances on the parts, the periscopes are designed to have accessible and adjustable primary mirrors in each of them, allowing co-alignment of the three solar lines of sight (see Figure 2). In fact all lines of sight are aligned with respect to NOMAD's main alignment cube, sitting on the –Y-face of the SO base plate (see Figure 25). This cube will also be used during integration on the spacecraft for checking the misalignment with the spacecraft's mechanical axes. This misalignment is important during flight when the pointing direction of the spacecraft has to be calculated.

Thermal Environment

Geometrical and Thermal Model

An instrument on an interplanetary mission, and especially on ExoMars where the payloads are exposed to open space, can be subject to extreme thermal environmental conditions. Following cases have been studied: a cold survival case during cruise phase, a cold non-operational case during the long eclipse right after Mars orbit insertion, a hot aerobraking case, and the standard hot and cold operational cases during science phase. For all of these cases temperature predictions have been made in a CAD model based thermal and geometrical mathematical model (TMM/GMM) (ESATAN TMS). In this model all external and internal elements impacting the thermal behavior of NOMAD have been taken into account.

External factors are the radiative and conductive coupling with the spacecraft, the neighboring instruments and the space environment (deep space, Mars, Sun at different ß-angles, aerobraking flux) at NOMAD's thermal interfaces, i.e. the three low conductance feet, the multilayer insulation (MLI), the radiator and the optical apertures.

The three interface feet of NOMAD have to fulfil a very stringent thermal conductance requirement (≤0.02 W/K) . Thermal conductance tests were performed (Mechanical Systems Laboratory, Thermal Division, ESTEC, The Netherlands) on a sample foot showing values between 0.022 W/K @ -43 °C and 0.036 W/K @ 26 °C per foot (uncertainty margin 8%). This non-compliance with the requirement has been assessed and accepted by ESA. Except for the radiator and the entrance apertures, NOMAD is completely wrapped in MLI with a twelve layer lay-up including XC100/VDA kapton black layers at inside and outside (solar absorptivity α_{MLI} = 0.93, infrared emissivity ε_{MLI} = 0.84) (manufactured by HPS, Germany and HPS, Portugal). The thermal blanket consists of nine individual pieces matching together and to the spacecraft MLI. The MLI is designed for continuous working at temperatures between -200 °C and +150 °C, and for surviving instant peak temperatures up to +392 °C. The radiator is covered by a 120 µm layer of SG121FD silicone paint (MAP, France) for optimal heat rejection (solar absorptivity α_{rad} = 0.27 ± 0.02, infrared emissivity ε_{rad} = 0.88 ± 0.03 @ +20 °C and 0.77 ± 0.03 @ -182 °C). The sizing of the radiator's surface area (9.011 dm^2) was driven by the need to cool down the instrument as much as possible (reduction of thermal background, especially in LNO) at one side, and by the restriction to not pass the lowest acceptable non-operational temperature for sensitive elements as e.g. the two AOTFs.

Internal thermal factors are the material and surface properties, the conductive boundary conditions between parts (0.38 mm thick Chotherm-1671 is used as thermal filler), the internal power dissipation during nominal operation (38.1W average and 47.9 W peak, independent of voltage) and power dissipation distribution during operational hot cases, the operational heaters (14.4 W, controlled by SINBAD during operational mission phases) and the survival heaters (16 W @ 22 V, controlled by independent thermostats with switch-on at -15 °C and switch-off at -10 °C during survival phases).

The model shows that for the coldest case (long eclipse) the survival heater power of 16W keeps all temperatures within limits, provided that the heater power distribution is adapted to the temperature gradient inside the instrument (more power near coldest parts). From the model it is seen that in the cold operational case, all temperatures are within limits and hence the operational heater powers are superfluous, unless one of the channels would remain switched off. In the hot operational case the temperatures in the electronics boxes tend to exceed their limit value of +50 °C.

If this worst case situation would appear during flight, an ultimate mitigation could be to keep the internal power dissipation lower by letting the channels work alternatively.

A sensitivity analysis has been performed looking at potential impact of variation in thermal parameters (α_{rad}, ε_{rad} and area of the radiator, thermal capacity and conductivity, power dissipation, contact resistance, MLI conductance) between the uncertainty boundaries. None of the parameter variations leads to worrying increase or decrease in the model temperatures.

Thermal Tests

Qualification level thermal balance and thermal cycling tests in a vacuum environment have been performed on the STM (CSL, Belgium). The STM is fully representative for the thermal behavior of the flight model (identical radiator and MLI, operational and survival heater chains present plus a separate heater chain to simulate the internal power dissipation). The test results obtained with the STM have been correlated with the mathematical model predictions. The thermal tests are repeated at acceptance level on the proto flight model.

From an optical point of view, the ideal working temperature is between -5 °C and +5 °C because optics are optimized for this temperature range. For SNR reasons the lower the temperature, the better.

Thermal Background, Signal and Noise

The signal-to-noise ratio (SNR) defines the sensitivity of an instrument. Especially in the LNO-channel during nadir observations, where the expected incoming signal is 10^6 times weaker than in LNO or SO during solar occultation measurements, suppression of the system noise is important. One of the most important sources of noise is the thermal background, that is highly temperature dependent. The higher the temperature of the instrument, the higher the thermal background. A broad range of parameters have an influence on the SNR, acting either on the portion of incoming signal that reaches the detector (*S*), the thermal background (*TB*) or on the noise (*N*). The F-number of the optics defines the amount of light collected and hence the signal intensity. A good matching between the F-numbers of the optics and the detector is advantageous for the SNR. In SO there is a mismatch (f/5.12 for the optics, f/3.936 for the detector) resulting in the detector seeing also part of the walls. In LNO this has been prevented by equalizing the F-number to f/3.936 over the whole chain. An additional advantage is that in LNO the height of the slit could be increased to cover the full etendue of the system (150' in LNO against 30' in SO). At the same time the slit in LNO has been made wider (4' in LNO against 2' in SO). The signal will be influenced also by the bandwidth and the diffraction efficiency of the AOTF. For LNO the bandwidth is slightly larger than for SO (24 cm^{-1} against 22 cm^{-1}) while the attainable diffraction efficiency with an RF power up to 2 W is somewhat lower (62% in LNO against 86% in SO). Likewise the transmission of the grating impacts the signal. The diffraction efficiency of the grating varies over wavelength and hence is different from order to order and, due to the dispersion inside one order, also from pixel to pixel. The SNR can be up to four times lower at the edges of the free spectral range (or the detector array) compared to the central pixel. Another important element is the cut-off wavelength of the detector. In LNO this cut-off is different from the one in SO (3.9 µm against 4.2 µm) due to the presence of a cold filter. Finally, the SNR can be significantly improved by reducing the thermal background, i.e. by cooling the optical and mechanical elements that are within the field of view of the detector.

The LNO-channel was initially designed to have a cooled spectrometer section (-100 °C), but the design was abandoned in a late stage, due to weight limitation issues. One additional obstacle was the fact that, even with a cooled spectrometer in front of the detector, the detector window itself remained still at high temperature, and would undo largely the gain obtained by the cooling. This means that the initial goals of an overall SNR during LNO nadir observations of ≥400 and a maximum of ≥1000 in the methane band cannot be met.

For the calculation of the incoming signal during solar occultations the spectral radiance of the Sun $L_{\lambda s}$ is used, which is independent of the position of Mars [29]. For nadir observations however the spectral irradiance of the Sun at Mars $E_{\lambda m}$ is used:

$$E_{\lambda m} = \frac{\pi . R_S^2}{D^2} . L_{\lambda s} \quad \textit{(Equation 12)} ,$$

with R_S the radius of the Sun and D the distance Mars-Sun. Hence, this spectral irradiance depends on the position of Mars with respect to the Sun. From $E_{\lambda m}$ the spectral radiance $L_{\lambda m}$, emitted by the Martian disk, can be derived:

$$L_{\lambda m} = \frac{A}{\pi} . E_{\lambda m} \quad \textit{(Equation 13)} ,$$

where A is the albedo of Mars. The signal level on the detector is calculated by applying the channel's transmission function to the incoming signal. The instrument transmission function is derived for each pixel across the detector array and each grating diffraction order as the product of the above described optical parameters of optics, grating and AOTF. For SO the signal on the detector can be expressed as:

$$S_\lambda = \frac{a.\pi}{4.F^2} . \Delta\omega . W_{slit} . T_{opt}(\lambda) . L \quad \textit{(Equation 14)} ,$$

with F the channel's F-number, a the pixel area, $\Delta\omega$ the pixel bandwidth (or spectral sampling interval, *SSI*), W_{slit} the slit width, $T_{opt}(\lambda)$ the transmission of the optics and L the radiance ($L = L_{\lambda s}$ for SO and $L = L_{\lambda m}$ for LNO). The signal S received on a detector pixel in e^-/s is given by:

$$S = \frac{\lambda}{h.c} . T_{\det}(\lambda) . QE . S_\lambda \quad \textit{(Equation 15)},$$

with λ the wavelength corresponding to the pixel, h Planck's constant, c the light velocity, QE the quantum efficiency of the detector and $T_{det}(\lambda)$ the sensitivity of the detector at the given wavelength.

All optical and mechanical elements that are entirely or partly 'seen' by a pixel, contribute to the thermal background *TB* received by that pixel. The thermal background, i.e. the number of thermal photons generated by an element, is calculated based on the temperature dependent thermal emission (Planck black-body equation), the emissivity and transmission of that element, and its etendue as viewed from the pixel. All elements situated in the optical path in front of the AOTFs are contributing very marginally to the thermal background, due to the filtering function of the AOTF. Only thermal background emitted in the selected passband of the AOTF can reach the detector. For the elements between AOTF and spectrometer slit the emitted thermal background is diffracted by the grating. Diffracted thermal background from all the grating orders will sum up on a pixel. For all elements after the spectrometer slit (slit included) the full thermal background (i.e. all wavelengths)

will be detected by a pixel. The thermal background, expressed in e^-/s, is obtained by introducing the quantum efficiency of the detector.

The noise *N* of the channels is the sum of different noise contributions:

$$N = N_{dark} + N_{ro} + N_{quant} + N_{shot} + N_{tb} \quad \textit{(Equation 16).}$$

The dark current noise N_{dark} and pixel electronics read-out noise N_{ro} are both fixed noises and given in the datasheet of the MARS MW detector (6000 e^-/s resp. 1000 e^-/pixel). The quantization noise N_{quant} is the noise that originates from the fact that the signal is digitized over a limited number of bits *n* (*n = 14* for NOMAD) and is higher for higher signal *S* and thermal background *TB*. The shot noise N_{shot} is the noise resulting from the signal impacting the detector (square root of *S*), the Johnson noise N_{tb} is the noise in the detector produced by the thermal background (square root of the thermal background *TB*). Equation 16 can be written as:

$$N = \frac{S + TB}{\sqrt{12}.2^n} + \sqrt{S} + \sqrt{TB} + Cte \quad \textit{(Equation 17)} .$$

The SNR of a detector pixel in the NOMAD channels is obtained taking into account all of the above signal and noise sources. The SNR depends on the time the pixel is exposed to the signal and the noise sources. Therefore an integration time has to be chosen that keeps the total charge below the saturation limit of the pixel, i.e. below its full well capacity ($14.8.10^{-6}$ or 36.10^{-6} e^- depending on the gain setting).

Figure 29 gives the SNR values for the SO and LNO-channels, at the central wavelengths of the orders, for typical integration times and for three different temperatures (263 K, 273 K, 283 K). For SO and LNO in solar occultation mode the figure gives the single pixel SNR values (no binning, no accumulations). In the LNO-channel working in nadir mode the pixels from one detector column have been binned over the slit height (144 pixels) and individual spectra have been accumulated over the duration of a measurement (15 s). Hence, for LNO in nadir mode the values in Figure 29 are the single pixel SNR values multiplied by the square root of the binning factor and the square root of the number of accumulations. The SNR can vary quite significantly over the pixels in a row (or over the columns in the detector).

Optical and Spectral Performance

Image Quality of the Slit Image on the Sun

A section of the observed source (Sun, Mars) is imaged on the spectrometer slit by the optics in front of the slit. To assess the image quality of these optics it is investigated how, inversely, the slit is imaged on the source. During nadir measurements (LNO), where a measurement lasts typically 15 s and the spacecraft moves with a relative ground velocity of 3 km/s, smearing will occur and a good image quality is not crucial. During solar occultation measurements however a sharp image of the slit is needed (only the central 24 lines are used) with good image quality perpendicular to the slit (Y-direction). The modulation transfer function (MTF) of a system indicates how 'faithfully' a subject (a line pattern expressed in cycles/mm) is transferred to its image by the system and, hence, is a measure for the image quality.

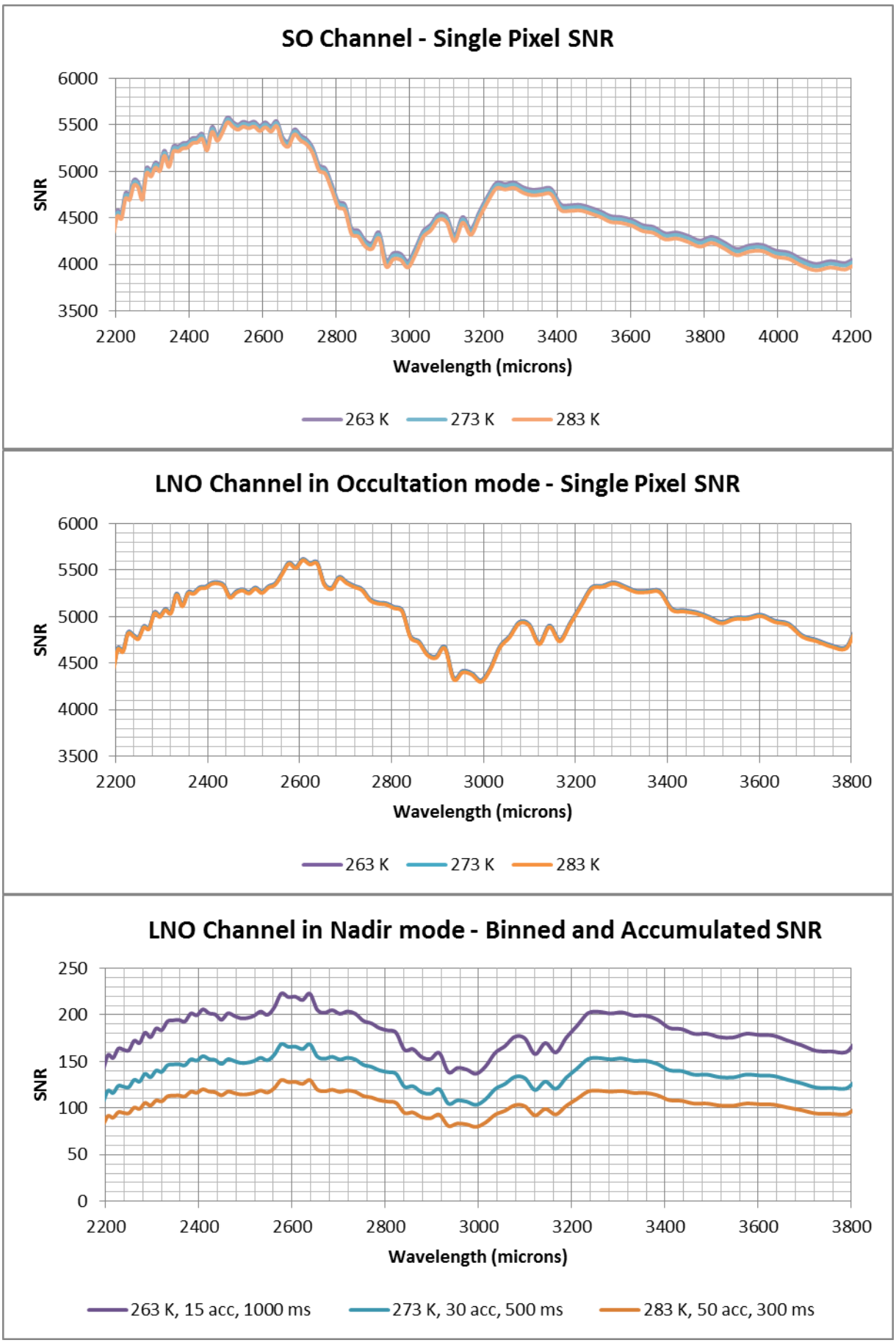

Figure 29. Top: single pixel SNR in SO (8 ms integration time). Middle: single pixel SNR in LNO (solar occultation mode) (2.5 ms integration time). Bottom: SNR in LNO (nadir mode) (144 pixels binned, see legend of plot for integration time and number of accumulations).

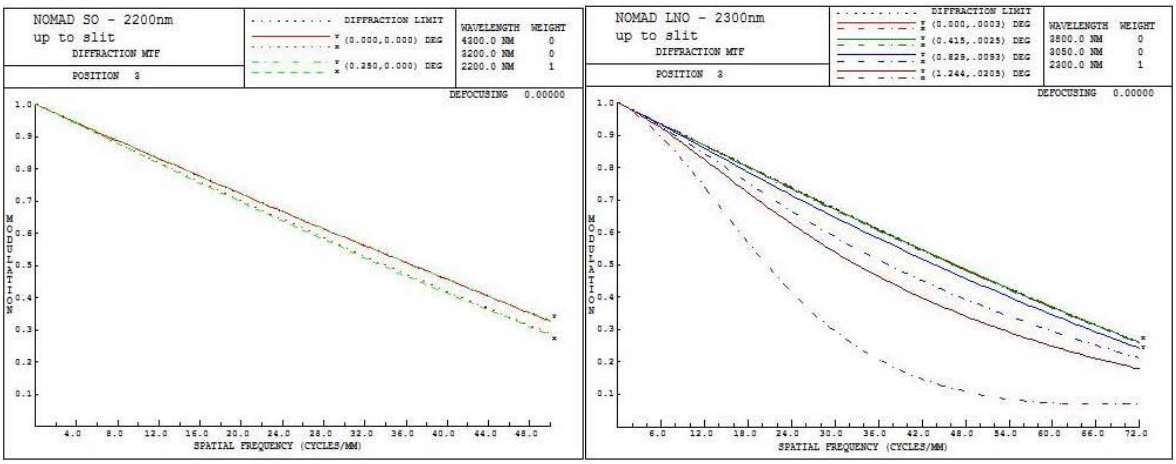

Figure 30. MTF for optics in front of spectrometer slit. Left: SO, 2.2 µm. Right: LNO, 2.3 µm.

It is seen in Figure 30 that for SO the MTF of the optics is close to being diffraction-limited (i.e. only limited by the wave nature of the light itself and the finite diameter of the optical elements) for all wavelengths and for all positions in the slit. For LNO the optics are also close to diffraction-limited but show some deviation at lower wavelengths (e.g. 2.3 µm) for positions close to the edges of the slit in the Y-direction and away from the center in the X-direction (parallel to the slit).

By convoluting the optics' point spread function (PSF) (i.e. the image the system makes of a point source) with a step function representing the geometrical size of the slit, the intensity profile of the image on the Sun is obtained. Figure 31 shows that this profile is 2' (SO) resp. 4' (LNO) wide (FWHM) corresponding nicely to the respective widths of the NOMAD slits.

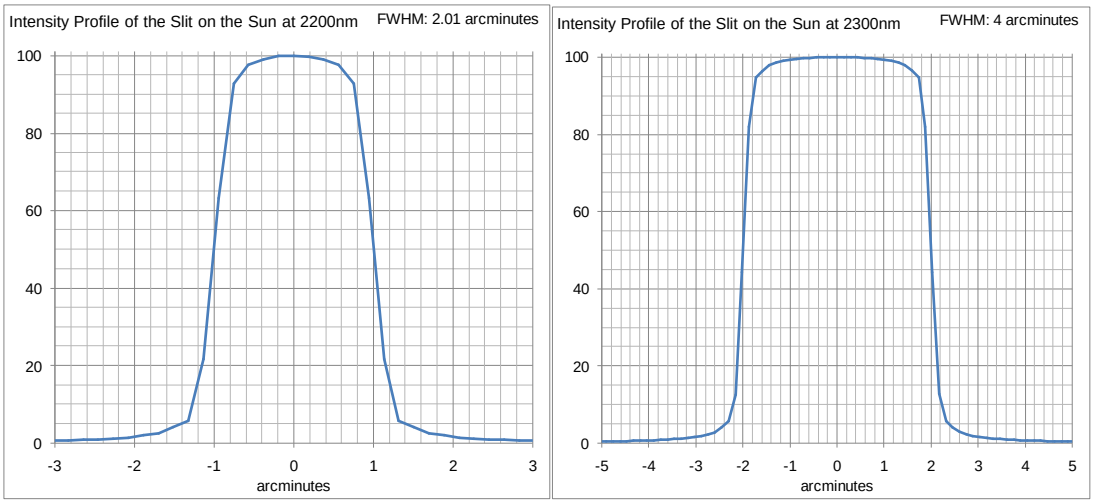

Figure 31. Intensity profile of slit image on the Sun (left: SO, right: LNO) at 2.2 µm resp. 2.3 µm.

Image Quality on the Detector

The optics between slit and detector form an image of the slit on the detector that is spectrally dispersed. To define the image quality in the Y-direction (i.e. the direction perpendicular to the slit) only the optics between slit and detector have to be taken into account, since in that direction the optics in front of the slit serve only to illuminate the slit (the object is a point source at the slit). In the X-direction (i.e. the direction along the slit) the image quality depends on the complete optics from

entrance till detector (the object is a point source at infinity in front of the instrument). The MTF at the focal plane position of the SO and LNO detector is calculated for both the spectral Y-direction and the spatial X-direction and plotted in Figure 32 for the central wavelength λ_c (corresponding to the center of the detector) in only one order (104 for SO, 117 for LNO), for different positions on the slit and up to the Nyquist frequency of the detector (16.7 cycles/mm). Similar plots can be obtained for all other orders and for wavelengths imaged at the edge of the free spectral range of an order or at the edge of the detector. In SO the MTF at the Nyquist frequency and at the central wavelength λ_c is always ≥0.4 in both the X- and the Y-direction. In LNO it is lower especially towards the edges of the slit (0.17 for the Y-direction) and the edges of the illuminated zone (0.1 for the X-direction). On top of that, at the 'spectral' edges (and especially at the low wavelengths in the orders) the image quality degrades further (0.18 in SO and 0 in LNO).

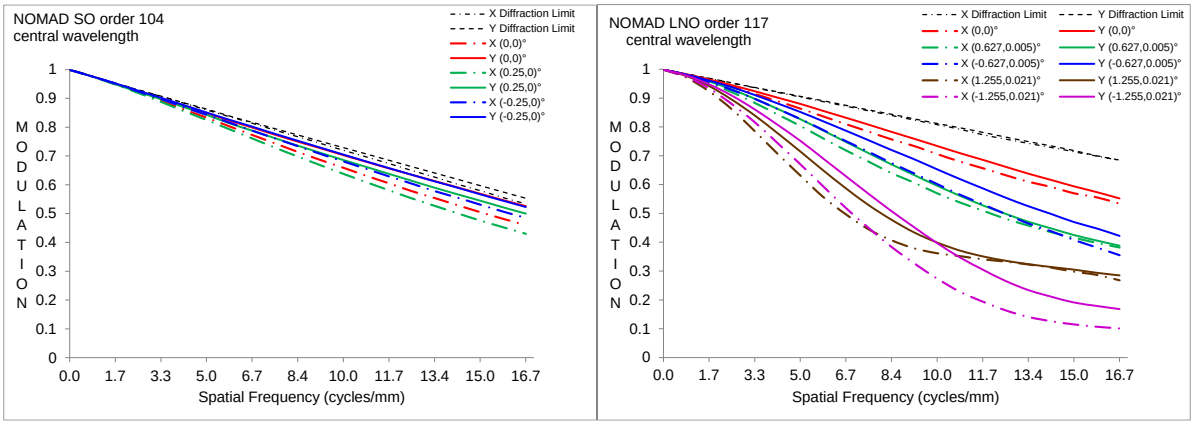

Figure 32. MTF for optics between spectrometer slit and detector. Left: SO, order 104, central wavelength 4.26 µm. Right: LNO, order 117, central wavelength 3.77 µm.

Smile and frown

Smile occurs in a spectrometer when its slit is not imaged as a straight line on the detector and, as a consequence, pixels in one detector column see slightly different wavelengths. A point source at the center of the spectrometer slit is imaged, for a specific wavelength, through the point spread function (PSF) of the system, as a spot on the detector. The center of this spot is used as zero reference for the smile. Other points on the slit, away from the center along the X-direction, are imaged on the detector but can deviate in the Y-direction from the zero reference. The Y-difference between the center of a spot and the center of the reference spot, all for the same wavelength, is a measure of the smile. It can be expressed in pixels or in cm^{-1} after conversion by means of the spectral sampling interval, that varies over orders and over pixels inside an order. In SO the smile at a given wavelength is always ≤0.1 pixels. In LNO the smile over the central 24' (solar occultations) is ≤0.15 pixels while over the full slit height of 150' (nadir) it is ≤0.8 pixels. In LNO a curved slit is used to compensate for the smile (see above).

Frown occurs when a specific point in the optical field is not imaged at the same height (i.e. in the same row) on the detector for all wavelengths. A point source in the field of the instrument is imaged, for the central wavelength λ_c of a specific order, as a spot on the detector. The center of this spot is used as the zero reference for the frown. For the same point in the field, but for other wavelengths in that same order, spots are formed at the detector that can deviate in the X-direction from the zero reference. The X-difference between the center of a spot and the center of the reference spot, all for the same field point, is a measure for the frown. In SO the frown for a given

field point in a given order is always ≤0.5 pixels. In LNO the frown for field points situated in the central 24' (solar occultations) is ≤0.65 pixels, while for field points situated in the full 150' (nadir) it is ≤1.8 pixels.

Instrument Line Profile

The instrument line profile (ILP) of a system is the energy distribution on the detector when the spectrometer slit is completely illuminated with monochromatic light. The theoretical ILP that can be expected based on the grating parameters, is obtained by multiplying the dispersion (Table 8 and Table 9) with the width of the spectrometer slit (60 µm in SO, 120 µm in LNO). The results are given in Table 13 and Table 14. The predicted ILP for the full NOMAD channels is obtained in three steps: (1) calculate the point spread function (PSF) of a point source in a number of positions along the height of the slit (or the useful part); (2) make the convolution of these PSFs with a square step function representing the geometrical size of the slit; (3) sum the Y-components of the convolution results. For LNO in nadir mode, where the used part of the slit is quite high, an additional step is needed, correcting for the smile of the system. Figure 33 gives an example of an instrument line profile for SO and LNO for the central wavelength λ_c in order 140 for SO and order 145 for LNO.

Table 13 and Table 14 give a broader overview of the ILP values (FWHM) for the central wavelengths in the orders in SO resp. LNO, as well as the fraction of the total energy within FWHM and within 2 pixels (SO) or 4 pixels (LNO), taking into account the manufacturing tolerances. For SO the ILP (FWHM) varies between 0.116 cm^{-1} or 63.21 µm (order 100) and 0.226 cm^{-1} or 62.3 µm (order 200) with energy fractions in 2 pixels between 77 and 84 %. For LNO the ILP (FWHM) varies between 0.247 cm^{-1} or 123.56 µm (order 120) and 0.454 cm^{-1} or 122.46 µm (order 200) with energy fractions in 4 pixels between 81 and 83%. The ILP (FWHM) for the wavelengths at the edge of the detector are slightly different from those in the center and the corresponding energy fraction is decreased at the edges by ≤5 %.

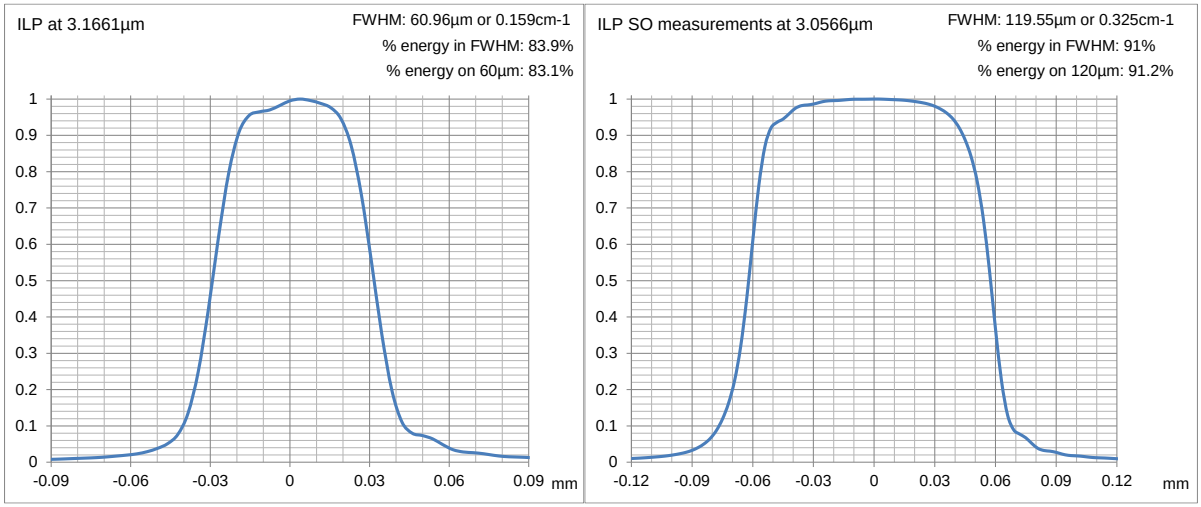

Figure 33. ILP for the central wavelength in order 140 (SO, left) and order 145 (LNO, right).

Table 13. Dispersion, theoretical ILP, predicted ILP, energy fraction for central wavelengths λ_c in SO.

Order	λ_c [µm]	$\partial\lambda/\partial D$ [cm^{-1}/mm]	Theoretical ILP (FWHM) [cm^{-1}]	Predicted ILP (FWHM) [cm^{-1}] – [µm]	Energy fraction in FWHM resp. in 2 pixels [%] – [%]
100	4.4302	1.88	0.113	0.116 – 63.21	78.79 – 77.12
110	4.0275	2.07	0.124	0.128 – 63.12	79.40 – 77.82
120	3.6919	2.25	0.135	0.139 – 63.02	80.01 – 78.52
130	3.4079	2.44	0.146	0.150 – 62.92	80.62 – 79.22
140	3.1661	2.63	0.158	0.161 – 62.82	81.22 – 79.92
150	2.9535	2.82	0.169	0.173 – 62.72	81.83 – 80.62
160	2.7689	3.01	0.181	0.184 – 62.63	82.44 – 81.31
170	2.6060	3.19	0.191	0.195 – 62.53	83.05 – 82.01
180	2.4612	3.38	0.203	0.206 – 62.43	83.66 – 82.71
190	2.3317	3.57	0.214	0.218 – 62.33	84.27 – 83.41
200	2.2151	3.76	0.226	0.229 – 62.24	84.88 – 84.11

Table 14. Dispersion, theoretical ILP, predicted ILP, energy fraction for central wavelengths λ_c in LNO.

Order	λ_c [µm]	$\partial\lambda/\partial D$ [cm^{-1}/mm]	Theoretical ILP @FWHM [cm^{-1}]	Predicted ILP @FWHM [cm^{-1}] – [µm]	Energy fraction in FWHM resp. in 4 pixels [%] – [%]
120	3.6914	2.26	0.271	0.247 – 123,56	81,59 – 80.79
130	3.4076	2.44	0.293	0.296 – 123,42	81,77 – 81.02
140	3.1641	2.63	0.316	0.319 – 123,28	81,95 – 81.26
150	2.9531	2.82	0.338	0.341 – 123,15	82,13 – 81.49
160	2.7686	3.01	0.361	0.364 – 123,01	82,31 – 81.73
170	2.6057	3.20	0.384	0.386 – 122,87	82,50 – 81.97
180	2.4609	3.39	0.407	0.409 – 122,73	82,68 – 82.20
190	2.3314	3.57	0.428	0.431 – 122,60	82,86 – 82.44
200	2.2148	3.76	0.451	0.454 – 122,46	83,04 – 82.67

Verification with Laser

The predicted instrument line profile was checked in the lab with a diffused collimated laser light beam (at 3.39 µm) filling the spectrometer slit entirely for SO. For LNO a patchwork filling of the slit was performed over more than 100 rows. Figure 34 shows the ILP in detector row 132 for SO and the averaged ILP for LNO over all illuminated rows. For SO the ILP in row 132 is 63.92 µm (2.13 pixels), with an energy fraction of 70.5% in the 2 central pixels, to be compared with the predicted values of 62.9 µm and 79.4%. For LNO the averaged ILP is 124.6 µm (4.15 pixels), with an energy fraction of 75.7% on the 4 central pixels, to be compared to a predicted average values of 123.0 µm and 81.7%.

Because the source contains only light at one wavelength, a single image of the slit should appear on the detector, rather than a horizontal band. Figure 35 gives the energy fraction in the central two pixels for all 30 rows (for SO) and in the central 4 pixels for the middle 108 rows (for LNO) that are illuminated by the respective slits, proving that the slit is imaged on the detector as expected.

Figure 36 gives for SO and LNO the position of the peak (column number scale) for each detector row. From these plots it can be seen that in both channels no smile is observed. One can however see a small tilt of the slit image with respect to the detector columns. In SO this tilt is 0.153 pixels over the total slit height of 30 pixels, in LNO it is 0.71 pixels over 80 central pixels (measured) and 1.32 pixels over the total slit height of 150 pixels (extrapolated).

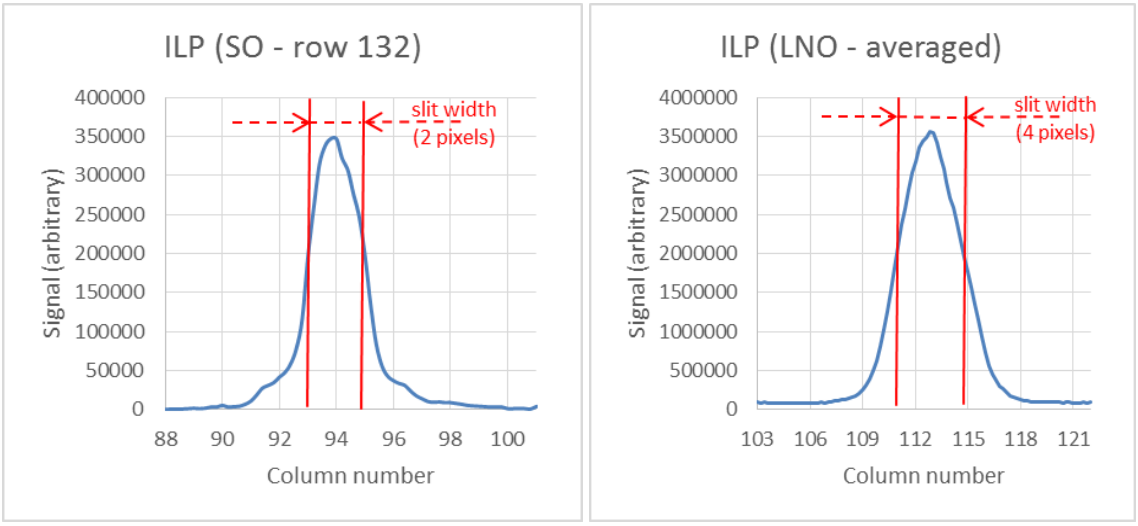

Figure 34. ILP for detector row 132 (SO, left) and averaged over 100 rows (LNO, right) with slit illuminated by monochromatic laser light beam at 3.39 µm.

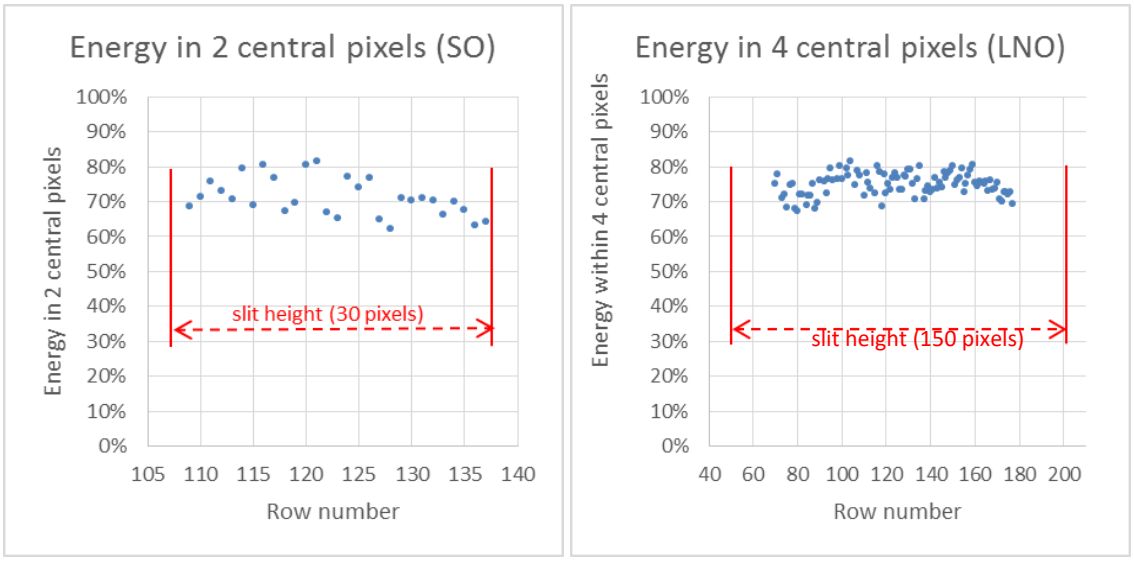

Figure 35. Energy fraction in the 2 central pixels (SO, left) and 4 central pixels (LNO, right) over the slit height with monochromatic laser light beam at 3.39 µm.

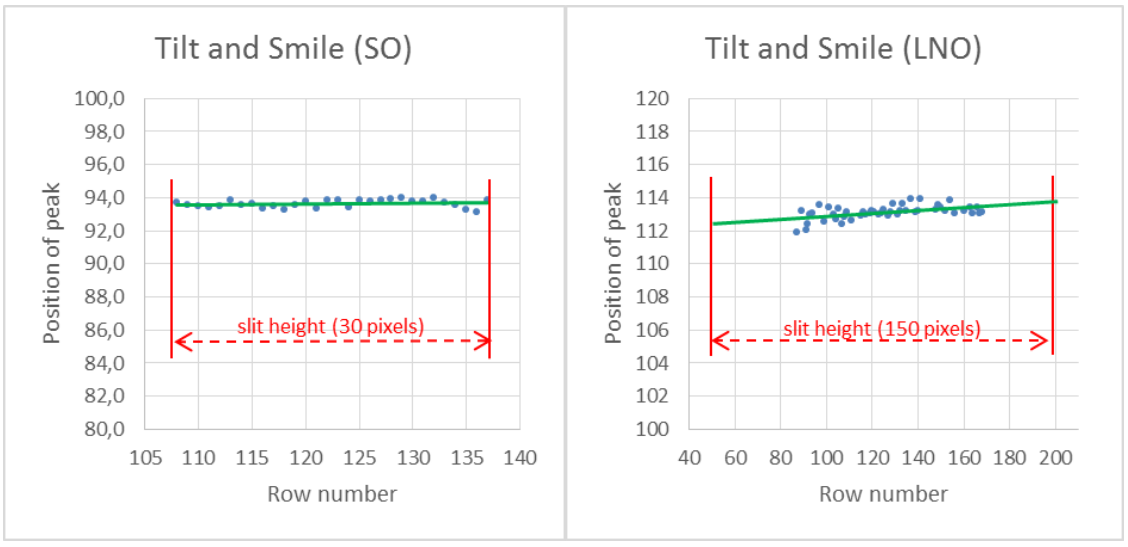

Figure 36. Position of peak as a function of row number (measure for tilt and smile of the optical system). Measured with monochromatic laser light beam at 3.39 µm (SO - left and LNO - right).

Verification with Broad Light Source

Both the SO and LNO channel was tested in a clean room environment with a broad infrared light source. In Figure 37 typical absorption spectra of the air in the lab are shown for one specific order (order 160 for SO @ AOTF frequency 21.68 MHz, order 168 for LNO @ AOTF frequency 24.31 MHz). The plots show 24 spectra, corresponding to individual detector lines in SO and to bins of 6 detector lines in LNO. At the time of this measurement the instrument was not yet calibrated, hence the figures are just qualitative indications of the good functioning of the infrared channels. Extensive reporting on instrumental calibration is the subject of a separate paper [28].

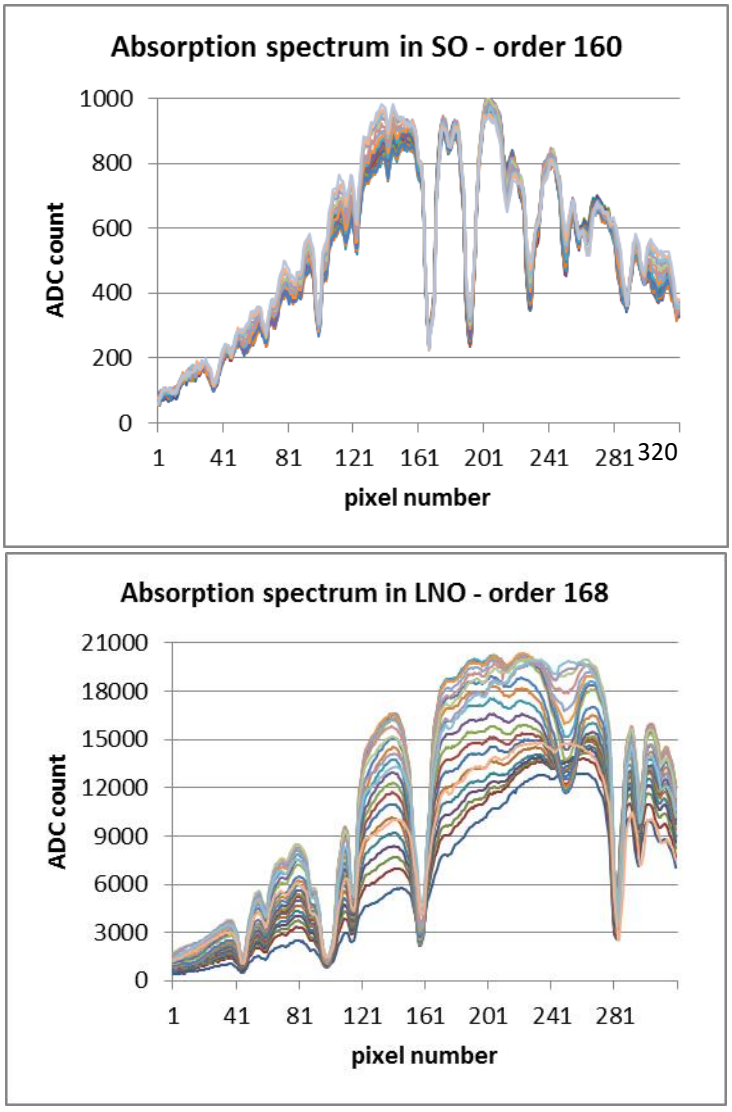

Figure 37.Absorption spectra with SO (top, order 160) and LNO (bottom, order 168) of ambient air, registered with a broad infrared light source.

Conclusions

In the conclusion of the paper that described the SOIR instrument on Venus-Express [1] the following statement was made. "It is obvious that the field of applications for the spectrometer described is not limited to the Venus-Express mission only. It could be extremely useful to study the presence of methane in the Martian atmosphere by solar occultation, and this spectrometer could perform such a task with a 10-times-higher spectral resolution than is possible with present instruments in orbit

around Mars." With the Trace Gas Orbiter of ExoMars, to be launched in January 2016, ESA offered a wonderful occasion to achieve this goal. This is why the first objective during the conception of NOMAD was to fly to Mars a one-to-one copy of the extremely successful SOIR instrument. The SO-channel of NOMAD, that is described in this paper, will offer good spectral resolution, high vertical sampling and excellent sensitivity during solar occultations.

While SOIR was limited to solar occultation measurements only, mass and volume settings for NOMAD allowed for a significant upgrade of the instrument. It was the goal to add, on top of the SO-channel, a second SOIR-like instrument, with more or less the same spectral characteristics but increased sensitivity, capable of performing measurements with much weaker light sources than the Sun (nadir, limb). Key element to come to this unprecedented performance was an extreme cooling of the spectrometer section to -100 °C. The LNO-channel, described in this paper, does not have this capability. The cryoradiator and spectrometer cryosection, the development of which was already far set, was descoped due to programmatic constraints and resource limitations. A suite of other measures has been taken to increase the signal-to-noise ratio of the LNO-channel so that nadir measurements with NOMAD will at least partially comply with the initial requirements.

All in all the NOMAD instrument, that besides the two infrared channels also contains a channel operating in the ultraviolet and visible wavelength range (not described in this paper), is bound to deliver Martian atmospheric science beyond the present knowledge thanks to a unique combination of spectrometric performances.

Acknowledgments

The NOMAD instrument has been developed under the responsibility of a Belgian principal investigator team (BIRA-IASB, Brussels), assisted by Co-PI teams from Spain (IAA-CSIC, Granada) and the United Kingdom (OU, Milton-Keynes). Associated teams contributing to the design and development of NOMAD were CSL (Liège, Belgium), IFSI (Rome, Italy) and IDR-UPM (Madrid, Spain). We thank all engineering and supporting personnel in these teams for the hard and solid work.

Several industrial partners were associated to the abovementioned teams. The industrial efforts were coordinated by a Belgian prime contractor (OIP, Oudenaarde). Following industrial associates, partners or subcontractors have contributed to NOMAD: AMOS (Liège, Belgium), Deforche (Izegem, Belgium), ERZIA (Santander, Spain), ESTEC (Noordwijk-aan-Zee, Netherlands), Glenair (Mansfield, United Kingdom), Gooch and Housego (Ilminster, United Kingdom), HPS (München, Germany), Lambda-X (Nivelles, Belgium), MAP (Pamiers, France), Protection des Métaux (Noisy le Sec, France), Sener (Barcelona, Spain), Sofradir (Grenoble, France), Thales Alenia Space Belgium (Charleroi, Belgium), Thales Alenia Space France (Conflans Sainte Honorine, France), Vaskon (Oudenaarde, Belgium).

An important part of the work described in this paper, and especially the outstanding optical design work, has been conducted by Wouter Moelans and Ludovic Aballea at OIP. Our gratitude also goes to Dennis Nevejans and Emiel van Ransbeeck, who, although retired, gave invaluable advice and support to the team at BIRA-IASB. Finally our deepest respect to Stefan Lesschaeve, system engineer at OIP, who sailed NOMAD safely through heavy weather.

We are very grateful to ESA for giving the scientific community the chance to go to Mars (once more) and for persisting when the project was in danger. Our warmest thanks to the ExoMars TGO project

team at ESA and especially to André Debus, who followed the development of NOMAD from start to finish.

NOMAD has been made possible thanks to funding by the Belgian Science Policy Office (BELSPO) and financial and contractual coordination by the ESA Prodex Office. **Funding in Spain, UK, Italy?**

References

[1] D. Nevejans, E. Neefs, E. Van Ransbeeck, S. Berkenbosch, R. Clairquin, L. De Vos, W. Moelans, S. Glorieux, A. Baeke, O. Korablev, I. Vinogradov, Y. Kalinnikov, B. Bach, J.-P. Dubois, and E. Villard, " Compact high-resolution spaceborne echelle grating spectrometer with acousto-optical tunable filter based order sorting for the infrared domain from 2.2 to 4.3 μm", Appl. Opt. 45, 21, 5191–5206 (2006).
[2] Mahieux, A., A.C. Vandaele, S. Robert, V. Wilquet, R. Drummond, F. Montmessin, and J.L. Bertaux, (2012). "Densities and temperatures in the Venus mesosphere and lower thermosphere retrieved from SOIR on board Venus Express: Carbon dioxide measurements at the Venus terminator." J. Geophys. Res. 117(E07001)
[3] Wilquet, V., R. Drummond, A. Mahieux, S. Robert, A.C. Vandaele, and J.L. Bertaux, (2012). "Optical extinction due to aerosols in the upper haze of Venus: Four years of SOIR/VEX observations from 2006 to 2010." Icarus 217(2): 875-881.
[4] Vandaele, A.C., A. Mahieux, S. Robert, R. Drummond, V. Wilquet, and J.L. Bertaux, (2014). "Carbon monoxide short term variability observed on Venus with SOIR/VEX." Planet. Space Sci. (in press)
[5] V. Formisano, V. I. Moroz, F. Angrilli, G. Bianchini, E. Bussoletti, N. Cafaro, F. Capaccioni, M. T. Capria, P. Cerroni, G. Chionchio, L. Colangeli, A. Coradini, A. Di Lellis, S. Fonti, R. Orfei, E. Palomba, G. Piccioni, B. Saggin, A. Ekonomov, A. Grigoriev, V. Gnedykh, I. Khatuntsev, A. Kiselev, I. Matsygorin, B. Moshkin, V. Nechaev, Y. Nikolsky, D. Patsaev, A. Russakov, D. Titov, L. Zasova, M. I. Blecka, A. Jurewicz, M. Michalska, W. Novosielski, P. Orleanski, G. Arnold, H. Hirsch, H. Driesher, J. Lopez-Moreno, R. Rodrigo, J. Rodriguez-Gomez, and G. Michel, "PFS: a Fourier spectrometer for the study of Martian atmosphere," Adv. Space Res 19, 1277–1280 (1997).
[6] R. Hanel, B. Schlachman, E. Breihan, R. Bywaters, F. Chapman, M. Rhodes, D. Rodgers, and D. Vanous, "Mariner 9 Michelson interferometer," Appl. Opt. 11, 11, 2625–2634 (1972).
[7] J.-L. Bertaux, et al., "The study of the Martian atmosphere from top to bottom with SPICAM Light on Mars Express," Planet. Space Sci., 48, 1303-1320 (2000).
[8] O. Korablev, J.-L. Bertaux, D. Nevejans, and the SOIR instrument team, "Compact high resolution IR spectrometer for atmospheric studies," Geophys. Res. Abs. 5, 14785 (2003).
[9] O. I. Korablev, J.-L. Bertaux, I. I. Vinogradov, Y. K. Kalinnikov, D. Nevejans, E. Neefs, T. Le Barbu, and G. Durry, "Compact high-resolution echelle–AOTF NIR spectrometer for atmospheric measurements," in *Proceedings of the 5th International Conference on Space Optics (ICSO 2004),* B. Warmbein, ed. ESA Spec. Publ. SP-554 (European Space Agency, 2004), pp. 73–80.
[10] O. Korablev, J.-L. Bertaux, I. I. Vinogradov, Y. K. Kalinnikov, D. Nevejans, E. Neefs, T. Le Barbu, G. Durry, A. Fedorova, and A. Grigoriev, "High resolution spectrometers for planetary spacecraft," presented at the 35th COSPAR Scientific Assembly, Paris, France, 18–25 July 2004.
[11] D. P. Baldwin, D. S. Zamzow, and G. P. Miller, "AOTF–Echelle spectrometer for Air-ICP-AES continuous emission monitoring of heavy metals and Actinides," in *Environmental Monitoring and Remediation Technologies,* T. V. Dinh and R. L. Spellicy, eds., Proc. SPIE 3534, 478–486 (1999).
[12] U.S. Department of Energy, "Compact high resolution spectrometer," Innovative Technol. Summary Rep. OST_TMS ID 1564 (U.S. Department of Energy, 2000).
[13] D. P. Baldwin, D. S. Zamzow, D. K. Ottesen, and H. A. Johnsen, "Testing of an echelle spectrometer as a LIBS detector at Sandia," Ames Laboratory Rep. IS-5148 (25 April 2001); www.osti.gov/bridge/servlets/purl/797630-w4wDHs/native/797630.pdf.
[14] O. Korablev and J.-L. Bertaux, "High-resolution IR spectrometer for the studies of planetary atmospheres," Geophys. Res. Abs. Geophys. Instrum. 3, 9492 (2001).
[15] O. I. Korablev, J.-L. Bertaux, and I. I. Vinogradov, "Compact high-resolution IR spectrometer for atmospheric studies," in *infrared Spaceborne Remote Sensing,* M. Strojnik and B. F. Andresen, eds., Proc. SPIE 4818, 272–281 (2002).
[16] European Space Agency, *Mars Express–The Scientific Payload,*ESA Spec. Publ. SP-1240 (European Space Agency, 2004), pp. 1–219.
[17] H. Svedhem, "Venus Express science requirements document," ESA document VEX-RSSD-SP-002 (European Space Agency, 2004).
[18] EXOMARS. Planetary Exploration Mission. Mars planet in-situ. smsc.cnes.fr/EXOMARS/OLD/GP_lander.htm.
[19] M. Patel, e.a., "NOMAD. An Integrated Suite of Three High-Resolution Spectrometers for the Infrared, Visible and Ultraviolet Domain for ESA's ExoMars Mission - Design, Manufacturing and Testing of the Ultraviolet Channel", in preparation.
[20] ExoMars Science Management Plan, EXM-MS-PL-ESA-00002, iss. 5, rev. 2 (2009).
[21] A. C. Vandaele, e.a., "NOMAD, a spectrometer suite for the ExoMars mission", in preparation.

[22] C. Palmer, *Diffraction Grating Handbook,* 6th ed. (Newport Corporation, 2005).
[23] M. C. Hutley, *Diffraction gratings*, Vol. 6 of Techniques of Physics (Academic, 1982), p. 76.
[24] B. W. Bach, Jr., K. G. Bach, M. Schulze, and B. Bach, Jr., "Modern echelons and echelles for infrared spectroscopy," in *Solar Physics and Space Weather Instrumentation*, S. Fineschi and R. Viereck, eds., Proc. SPIE 5901, 184–190 (2005).
[25] M. S. Gottlieb, "Acousto-optic tunable filters," in "*Design and Fabrication of Acousto-Optic Devices,*" A. P. Gotzoulis, D. R. Pape, and S. V. Kulakov, ed. Marcel Dekker, 197–283 (1994).
[26] I. C. Chang, "Non-collinear acousto-optic filter with large angular aperture," Appl. Phys. Lett. 25, 370–372 (1974).
[27] MARS MW 320x256 – 30 µm pitch – MCT. The reference for MWIR 320x256 detectors. www.sofradir.com.
[28] I. Thomas, e.a., "NOMAD, calibration of three spectrometer channels", in preparation.
[29] ASTM E490-00a(2014) Standard Solar Constant and Zero Air Mass Solar Spectral Irradiance Tables. www.astm.org.